MSc Thesis
Name student: Janssen. L.M (3613771)
Supervisors: Dr. A. Niemeijer, Dr. S. Hangx
Utrecht, 7 May 2016

Universiteit Utrecht
Faculty of Geosciences

The long term influence of CO_2 storage on the frictional strength of clay-rich rocks

Janssen, L.M. [1]

[1] Faculty of Geoscience, High Pressure and Temperature Laboratory, University of Utrecht, L.M.Janssen1@students.uu.nl

Abstract

Geological storage of CO_2 is a technology that could be a potential solution for the global issues of climate change and reducing CO_2 emissions. It is important to understand the long term influence of CO_2 storage on fault strength, the mechanical properties and stability of the surrounding rocks since key to successful implementation will be to ensure storage integrity on the long term. Study material derived from natural CO_2 reservoirs in Green River, Utah, showed bleached zones (devoided of hematite) in the Carmel Formation related to CO_2 penetration. Preliminary experiments suggested that small differences in mineralogy (and dissolution of hematite) could have significant influence on the frictional strength of rocks. Velocity stepping and normal load stepping experiments have been performed on a ring shear apparatus at room temperature, 120°C and 200°C, effective normal stresses of 20 - 50 MPa, sliding velocities of 1 – 100 μm/s and pore fluid pressure of 15 MPa on clay-rich samples containing 15 – 38% illite, 1 – 20% quartz, 0 – 3% hematite, kaolinite, dickite and phengite, and Carmel samples with and without hematite. The results show no significant difference in frictional strength on the illite clay samples with varying mineral composition and contents of hematite, with all clay samples varying between μ = 0.20-0.38. The Carmel samples, with higher quartz content, show μ = 0.55-0.61. The velocity dependence parameter (a-b) was positive for all illite clay samples indicating velocity strengthening behavior, the Carmel samples showed mostly negative values with the samples without hematite being the most negative, indicating velocity weakening behavior. The results imply that CO_2 storage has no clear, significant influence on the frictional strength of clay rich rocks, but could possible results in unstable slip caused by negative (a-b) values and velocity weakening behavior by the reduction of hematite.

Keywords: CCS; CO_2 storage; illite clays; hematite; rate and state friction; ring shear experiments

Contents

List of tables **3**

List of figures **4**

1. Introduction **5**

2. Theoretical background **8**

2.1 Friction of clays 8

2.2 Rate and State Friction theory 11

3. Materials and methods **13**

3.1 Sample material 13

3.1.1 Removing hematite - Sodium dithionite procedure 14

3.2 Sample analysis 15

3.2.1 Grain size analysis 15

3.2.2 XRD and ICP analysis 16

3.3 Sample preparation 18

3.4 Experimental apparatus and procedure 19

3.4.1 Velocity stepping experiments 22

3.4.2 Normal load stepping experiments 22

3.4.3 Normal load and velocity stepping experiments 22

3.5 Data processing 23

4. Results **25**

4.1 Mechanical Data 25

4.1.1 Velocity stepping experiments 25

4.1.2 Normal load stepping experiments 29

4.1.3 Carmel experiments – normal load and velocity stepping experiments 33

4.1.4 Velocity dependence of friction 36

5. Discussion **42**

5.1 Mineralogy quantification of the samples by XRD and ICP 42

5.2 Effect of mineralogy on the frictional properties 43

5.3 Effect of hematite on the frictional properties 44

5.4 Effect of type of experiment 45

5.5 Implications for CO_2 capture and storage (CCS) 50

6. Conclusion **53**

7. Acknowledgements **55**

8. References **55**

9. Appendix **58**

List of tables

Table 1: Mineralogy results for the 5 samples based on X-Ray Diffraction (XRD)....17
Table 2: Results of the Inductively Coupled Plasma (ICP) Mass Spectrometry analysis for 5 samples, values are given in ppm (mg/kg)....17
Table 3: Mineral composition of each sample based on X-Ray Diffraction (XRD) analysis and Inductively Coupled Plasma (ICP) mass spectrometry analysis. 18
Table 4: List of experiment names, sample material and corresponding conditions at which the experiments are performed.. 19
Table 5: List of experiment numbers, sample material and corresponding conditions at which the experiments are performed....24
Table 6: List of the linear relations between shear stress and effective normal stress for the velocity stepping experiments 28
Table 7: List of the linear relations between shear stress and effective normal stress for experiment normal load stepping experiments. 32
Table 8: List of the linear relations between shear stress and effective normal stress for the Carmel experiments....36

List of figures

Figure 1: Schematic diagram of the different clay fabrics....11
Figure 2: Rate and state dependent friction model. 13
Figure 3: Sample material used in this study in powder form....14
Figure 4: Sodium dithionite procedure using a magnetic stirrer at a temperature of 50°C. 15
Figure 5: Grainsize distribution for the red illite (RI1 and RI2) and white illite (WI1 and WI2) performed twice with a laser particle sizer....16
Figure 6: Photograph of the hydrothermal ring shear apparatus and pressure vessel loaded inside of the Instron loading frame....21
Figure 7: Evolution of the friction coefficient with shear displacement for the velocity stepping experiments u416 - u428). 27
Figure 8: Shear stress vs. effective normal stress for the velocity steps experiments (u416 – u428). 28
Figure 9: Evolution of the friction coefficient with shear displacement for (a) all normal load experiments u432 – u447 and for (b) all experiment on red illites....31
Figure 10: Shear stress vs. effective normal stress for the normal load stepping experiments 33
Figure 11: Evolution of the friction coefficient with shear displacement for the Carmel CCV-70A sample and the Carmel sample without hematite. 35
Figure 12: Shear stress vs. effective normal stress for the velocity- and normal stepping experiments of the Carmel samples (u448 and u450). 36
Figure 13: Results for modeling the constitutive parameters a, b (b_1 and b_2), Dc (D_{c1} and D_{c2}) and (a-b). 37
Figure 14: Values of the velocity dependence parameter *(a-b)* for the illite samples. 40
Figure 15: Values of the velocity dependence parameter *(a-b)* for the Carmel samples (u448 and u45). 41
Figure 16: Shear displacement (mm) versus shear stress of the seals (MPa) 47
Figure 17: Shear stress vs. effective normal stress for the normal load stepping experiment, showing the maximum uncertainty range based on the correction of the seal friction.. 49

1. Introduction

CO_2 capture and storage (CCS) is a technology where carbondioxide (CO_2) is captured at the source, transported and injected into depleted oil and gas reservoirs, deep saline aquifers, or unmineable coals seams (Bachu et al., 1994; Hitchon, 1996). This technology could be a potential solution for the global issue of climate change by reducing CO_2 emissions. To ensure storage integrity, it is important to understand the geochemical behavior of carbon dioxide storage in geological reservoirs over short (laboratory timescale (months) - years) and long (i.e. > 10 000 years) timescale.

Key to successful implementation of CCS technology will be to ensure storage integrity is maintained on timescales of > 10 000 years. Loss of integrity could occur via the potential leakage of CO_2 along pre-existing faults, and the potentially lead to induced seismicity (Zoback & Gorelick, 2012). However, the long term influence of CO_2 exposure on the surrounding rocks is still a process that is not well characterized, in particular potential effects of long term interactions between CO_2, brine and rock on the mechanical and transport properties on intact reservoir rock and caprock, as well as faults (Hangx, et al., 2015; Busch, et al., 2014). Short-term laboratory experiments on North Sea reservoir sandstones and caprocks have been performed to show that fault friction and slip stability are not affected by CO_2 exposure (Samuelson & Spiers, 2012). Since most CO_2/brine/rock reactions are very slow, even under typical in-situ conditions (T= 0-120 °C, effective stress = 10-50 MPa), they are difficult to simulate in the laboratory since the necessary timescales cannot be accessed in laboratory experiments. Possible reactions that could occur are results of the increased acidity (CO_3^{2-}) caused by the dissolution of CO_2 in water (i.e. the minerals dissolve). The reactions involve the dissolution of carbonate with CO_2 ($CaCO_3 + CO_2 + 2H_2O \rightarrow Ca^{2+} + 2HCO_3^-$), the dissolution of alumino-silicate, i.e. feldspar, (Ca and Na rich), mica and the dissolution of hematite (see also reaction 1-4 below). Other reactions involve the precipitation of clays (e.g. illite, kaolinite) and also carbonates by the presence of divalent cations ($CO_2 + 2H_2O + M^{2+} \rightarrow MCO_3 + 2H^+$) (Baines & Worden, 2004). The addition of CO_2 to the subsurface could theoretically lead to dissolution of carbonates as well as precipitation, depending on the reactive minerals in the rock (i.e. is pH buffered) (Baines & Worden, 2004).

One way of circumventing this issue is to study material derived from natural CO_2 rich reservoirs and to study the long term influence of CO_2 on fault strength and stability by variations in mineralogy in fault rocks expected from mineral reactions with CO_2. Examples of natural CO_2 reservoirs are the Werkendam field in the Netherlands and reservoirs in the Colorado Plateau near Green River, UT, USA (Hangx, et al., 2015; Kampman, et al., 2014). A recent study was performed on the reservoir-caprock system of a natural CO_2 complex near Green River, Utah

(USA) in order to provide constraints on the long-term influence of CO_2 charged fluids on storage integrity (Busch, et al., 2014). A drilling campaign obtained core through two CO_2-charged reservoirs of Jurassic Sandstones, called the Entrada Sandstone and Navajo Sandstone, as well as through the clay-rich caprock overlying the Navajo sandstone called the Carmel Formation. The caprock material, as well as the silty claystone in the Entrada Sandstone showed distinct bleaching zones related to CO_2-penetration (Busch, et al., 2014; Kampman, et al., 2014). The bleached zones in the silty claystones present in the Entrada Sandstone are about 10.4 cm thick and the mineralogy results showed that the siltstone layer consist on average of 39 wt.% of quartz and 39 wt.% of illite with minor contributions of K-feldspar, hematite, dolomite, albite and pyrite and some trace elements (Busch, et al., 2014). The bleached zones found at the base of the Carmel Formation, in contact with the CO_2-gas cap present in the underlying Navajo Sandstone, are about 5-10 cm thick and show alteration of the cap rock mineralogy. The mineralogy of the bleached zones showed that the zone was devoid of hematite, explaining the loss of its original reddish color (personal communication S. Hangx). Hematite dissolution occurred due to the acidity caused by the dissolution of CO_2 (reaction 1) and also the reducing environment (Fe^{3+} reduced to Fe^{2+}) created by CO_2 and minor quantities of H_2S dissolved into the reservoir water (reaction 2). At the same time dissolution of dolomite (reaction 4) and precipitation of pyrite (reaction 3) was observed in reaction profiles resulted from XRD and XRF measurements (Busch, et al., 2014; Kampman, et al., 2013). The following reactions are given by Busch, et al., 2014:

(1) $CO_2 + H_2O \Leftrightarrow H_2CO_3 \Leftrightarrow HCO_3^- + H^+$

(2) $4Fe_2O_3$ *(hematite)* $+ H_2S + 14CO_2 + 6H_2O \Leftrightarrow 8Fe^{2+} + 14HCO_3^- + SO_4^{2-}$

(3) $2HS^- + Fe^{2+} \Leftrightarrow FeS_2$ *(pyrite)* $+ 2H^+$

(4) $CaMg(CO_3)_2$ *(dolomite)* $+ 2H^+ \Leftrightarrow Ca^{2+} + Mg^{2+} + 2HCO_3^-$

Preliminary experiments on illite-rich (~80 wt.%) samples taken from the Carmel Formation, both with reduced hematite content (0-0.2%, bleached zone) and a higher hematite content (up to 5 wt.%, unbleached zone) showed that this small difference in mineralogy appeared to have a significantly influence on the frictional strength of the rock (Samuelson & Niemeijer, Unpublished results). The main question in this report then is: can small variations in mineralogy, in particular the presence or absence of hematite, have significant effects on fault strength? And if so, what is the underlying mechanism causing the difference in frictional strength of the rock?

One of the theories that could explain the difference in fault strength as determined in the preliminary experiments on illite rich samples and the samples with the reduced hematite content could be the effects of interparticle forces or flocculation of the clay particles with the presence of hematite. It is important to understand the behavior of clays and interparticle forces for clays and

different minerals (e.g. hematite) to explain any difference in frictional strength of the rocks. A theoretical background about the frictional behavior of clays and interparticle forces is given in section 2.1.

In this report, the long term influence of CO_2 storage on the frictional strength of clay-rich (cap) rocks, and in particular those rich in illite was investigated by performing friction experiments in a ring shear apparatus on clay samples with varying mineral compositions and contents of hematite. In addition, samples from the Carmel formation were tested to compare the results with the performed friction experiments on the illite-rich clays. The data obtained from the experiments will be used to derive a relationship between the composition, temperature and frictional strength. The variation in mineralogy will simulate varying mineral content in fault rocks in long term contact with CO_2-charged fluids and whether there is a difference between the samples with more hematite or not, i.e. whether long-term leaching of clay-rich faults with CO_2 can lead to weakening and/or a change in velocity dependence of friction. The rate- and state friction theory, see section 2.2, was used to investigate whether the presence or absence of hematite changes the velocity-dependence of friction, which we need to know to determine the seismogenic potential of faults (i.e. stable slip (creep) or unstable slip (earthquakes) along clay-rich faults capping potential CO_2-reservoirs (Ruina, 1983; Dieterich, 1978).

2. Theoretical background

In this section a theoretical background is given about the friction behavior of clays in general and the effect of mineralogy (in particular hematite) on the friction of clays. In addition, the effective stress law and rate and state friction (e.g. the velocity dependence of friction) will be explained to set the framework for discussing the experimental results obtained.

2.1 Friction of clays

To understand the influence of mineralogy and specifically the presence or absence of hematite on the friction behavior of clay rich rocks, it is necessary to first understand some background information about crystal structures and the friction of clay rich rocks in general.

According to Byerlee's rule the coefficient of friction for a variety of rocks is μ = 0.6 – 0.85 and a maximum coefficient of friction of μ = ~0.85 at normal stresses <200 MPa (Byerlee, 1978). However, the friction of sheet silicates is confirmed by several studies to be much lower than Byerlee's rule. The friction of clays typically varies between values of μ = 0.03 and μ = 0.50 for illite, smectite (montmorillonite and saponite) and chlorite (Ikari, Marone, & Saffer, 2009). For illite clays in general, other studies showed values of for example μ = ~0.41 – 0.63 (Saffer & Marone, 2003), μ = 0.4 (Morrow, Radney, & Byerlee, 1992) and μ = 0.2 – 0.5 for layer structure minerals (Moore & Lockner, 2004). The experiments in these studies are all performed at room temperature and effective normal stresses in the range of 5 - 150 MPa. The coefficient of friction of rocks typically decreases with increasing clay content at room temperature and effective normal stress of 40 MPa (Tembe, Lockner, & Wong, 2010). Existing studies have also conclusively shown that clay mixtures, including illite clay, generally show an increase in friction with increasing loading velocity, indicating velocity-strengthening behavior and a positive value of *(a-b)* in the framework of Rate and State Friction (RSF) described in section 2.2 (Saffer & Marone, 2003; Tembe, Lockner, & Wong, 2010).

The coefficient of friction depends on the presence and composition of pore fluids, shear rate, temperature and the type of mineral or crystal structure. Fluid pressure (P_f) for example, can significantly lower the effective stress, since $\tau = \mu\left(\sigma_n - P_f\right) + S_0$ (Behnsen & Faulkner, 2012). The frictional strength of rocks increases with increasing temperature (at temperatures of 25 - 280°C) according to Moore & Lockner (2004). Den Hartog, et al., 2012, investigated the effect of temperature on illite gouges, the results showed a transition from velocity strengthening to velocity weaking behavior at temperatures of ~250°C.

The effective normal stress has an influence on the friction coefficient as well. In the study of (Behnsen & Faulkner, 2012) the effect of normal stress on the coefficient is investigated at normal stress of 5 – 100 MPa. The results of this study showed that shear stress increased with increasing effective normal stress. The friction coefficient is constant for higher effective normal stresses (>20 MPa) and at lower effective normal stresses (<20 MPa) the coefficient of friction increases, which is probably caused by the strength of the jacket and gouge cohesion (Behnsen & Faulkner, 2012). According to Den Hartog, et al., 2012, the coefficient of friction and slip hardening rate was found to increases weakly with normal stress.

But what is the effect of mineralogy on the friction of clays, and specifically, does the presence or absence of hematite have any effect on the coefficient of friction?

Effect of mineralogy - Clays and micas are groups within the sheet (phyllo-) silicates which are characterized by their basic structure of parallel sheets or platy crystals of silicate tetrahedral (Si_2O_5), stacked upon each other. A variety in layer charge, interlayer cations and isomorphous substitutions in minerals results in a wide range of crystal structures (Behnsen & Faulkner, 2012). Friction coefficients vary for different sheet silicates, depending on their crystal structure and the electrostatic bond energy or interlayer bonding energy between two basal surfaces (Behnsen & Faulkner, 2012; Moore & Lockner, 2004). The coefficient of friction (μ) is related to the shear strength (τ), see also equation 1 in section 2.2 where $\tau = \mu\left(\sigma_n - P_f\right) + S_0$, which can also be considered as the result from the difference between interparticle forces of attraction and repulsion, and type of the interlayer bonds (Warkentin & Yong, 1960). The coefficient of friction (dry) typically increases with increasing interlayer bonding energy up to separation energies of ~293 kJ/mol (or ~70kcal/mol). Sheet silicates have charged surfaces and since the minerals tend to absorb water, the frictional strength between the surfaces reduces in the presence of water because shear will be concentrated within the water layers. Therefore, phyllosilicates are always weaker when then are wet than dry. In general, the wet friction coefficient also increases with increasing separation energy (Morrow, Moore, & Lockner, 2000; Moore & Lockner, 2004). The strongest sheet silicate group is the 1:1 sheet silicate group, for example kaolinite, in which the layers are held together by hydrogen bonds (Moore & Lockner, 2004). The 2:1 sheet silicate group is generally weaker. There is also a difference between di-octahedral minerals (i.e. illite, montmorillonite, pyrophyllite and muscovite) and tri-octahedral minerals (i.e. talc, phlogopite and biotite). Di-octahedral sheet structures are generally stronger than tri-octahedral sheet structures (Morrow, Moore, & Lockner, 2000; Moore & Lockner, 2004; Behnsen & Faulkner, 2012), since the interlayer bonds of the di-octahedral minerals are somewhat stronger (two thirds

of the octahedral cation sites are filled with trivalent cations and the other third is empty, i.e. the layer distortion is higher (Giese, 1978)).

Effect of flocculation - Besides the mineral structure, the shear strength of clays depends on the microfabric of the particles as well. Interparticle forces may influence the shear strength, since forces can lead to a structure or particle arrangement that influence strength (Warkentin & Yong, 1960). The microfabric of clays can be either one of the two extremes, dispersed arranged (highly oriented particles) or flocculated arranged (randomly arranged particles). The type of microfabric depends on the depositional environment and the physical and chemical processes during a later stage (Pillai et al., 2010). Several studies have been done on the shear strength behavior of clays with different micro fabrics. Pillai., et al, 2010 found that due to the randomly arranged particles in the flocculated arrangement, flocculated samples have higher resistance and higher shear strength in direct shear (drained) test than dispersed samples where the particles are horizontally arranged (see Figure 1).

Effect of hematite - For this study the frictional strength of clay-rich rocks (and in particular rich in illite) will be investigated with samples of varying mineral compositions and content of hematite (Fe_2O_3), therefore it is important to understand if hematite in clays has any influence on the frictional strength in theory. Several studies have been done on the interaction of clay silicates and iron oxides to understand the influence on clay aggregation and the related physical properties, for example, flocculation and dispersion (Arias et al., 1995). With the aggregation of clay minerals, small clay particles, polymers or other small charged particles form irregular particle clusters or flocs (Figure 1). Earlier studies have concluded that ferric compounds (i.e. iron-containing compounds) play an important role in the aggregation of clay minerals, since the negative permanent charge of the basal surface of clay silicates will interact via coulomb attraction with the positive variable charge of the iron oxides (Arias et al., 1995; Blackmore, 1973; Michalet, Guillet, & Souchier, 1993). A study by Ohtsubo & Yoshimura (1991) on specifically the particle interaction of illite clay and iron oxides showed that the addition of 2 and 5% of iron oxide to illite clay causes the positively charged iron oxides to be adsorbed by the negative charge on the illite surface, which result in the illite surface to be partially neutralized. The electrostatic attraction between the two negative charged illite surface and the positive charged iron particles would cause flocculation of face-to-face association (Figure 1). This also leads, for the complexes with iron oxides of 2% and 5% as opposed to pure illite, to a greater degree of coagulation, greater particle-interaction forces and modes of particle association (also called: the Bingham yield stresses) (Ohtsubo & Yoshimura, 1991).

Summarized, clay minerals tend to flocculate more easily with the presence of hematite (iron-oxide particles) and since flocculated samples have higher resistance and higher shear strength, this could theoretically mean that samples containing ~2-5% hematite have higher shear strength and therefore a higher friction coefficient.

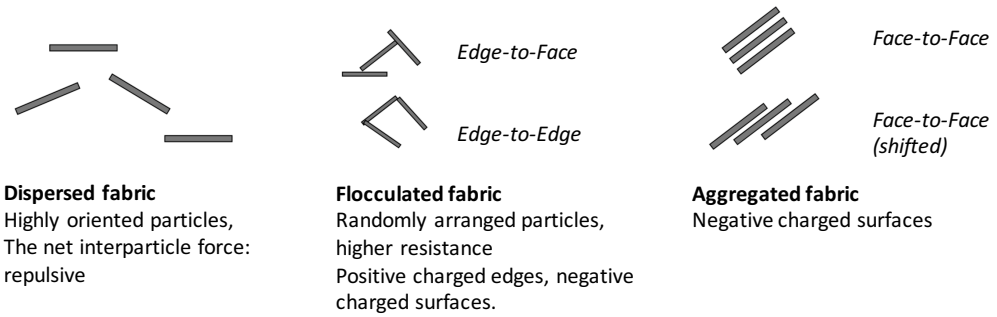

Figure 1: Schematic diagram of the different clay fabrics, including the dispersed (highly oriented particles) fabric, the flocculated fabric (randomly arranged particles), and the aggregated fabric, where the particles are attracted together face-to-face. Clay minerals tend to flocculate more easily with the presence of hematite.

2.2 Rate and State Friction theory

In order to understand the frictional strength of clay rich rocks, we first have to approach the effective stress law and the rate and state friction laws. Shear strength can be defined by the effective stress law (Coulomb or Byerlee type static failure envelop):

$$\tau = \mu \left(\sigma_n - P_f\right) + S_0 \quad (1)$$

where τ is the shear strength of the fault (Pa), μ is the coefficient of friction for the fault , $\sigma_n$is the normal stress (Pa), P_f is the pore fluid pressure (Pa) and S_0 is the cohesive strength, the resistance force per unit area, (≥0) (Pa) (Byerlee, 1978). In theory, failure or reactivation of a fault can be caused by the reduction of the shear strength through a decrease in friction coefficient μ or a change in the effective stress. Since slip on a fault zone can be induced by the reduction of the friction coefficient μ (even at constant pore fluid pressure), it is important to know if there is a possible long term influence of CO_2 on the strength and stability of faults and if the frictional strength of faults is reduced by small changes in mineralogy (Samuelson & Spiers, 2012). Once a fault is reactivated, we have to know the frictional stability of the faults (i.e. whether slip will be stable or unstable) by using the velocity dependence of friction.

The velocity dependence of friction of fault gouges is typically described using the rate and state friction (RSF) laws by (Ruina, 1983) and (Dieterich, 1981; Dieterich, 1978). The rate and state friction law with the empirical Dieterich type equation can be expressed as followed:

(2) $$\mu = \mu_0 + a \ln(\frac{V}{V_0}) + b \ln(\frac{V_0 \theta}{d_c}) \text{ with } \frac{d\theta}{dt} = 1 - \frac{V\theta}{d_c}$$

with: μ = coefficient of friction, μ_0 = coefficient of friction measured at velocity V_0, d_c = critical sliding distance, a = the magnitude of instantaneous change in μ upon a step change from sliding velocity V_0 to a value V, b = the magnitude of change in μ during subsequent evolution to a new steady state value over a critical sliding distance d_c (Marone, 1998).
The Dieterich law can be used to describe the evolution of the friction coefficient in response to changes in sliding velocity, which controls the mode of sliding. In the case of steady, the velocity dependence of friction can be quantified in a rate and state-dependent friction model, Figure 2, using the parameter:

(3) $$(a - b) = \frac{\Delta \mu_{ss}}{\Delta \ln V}$$

with: $\Delta \mu_{ss}$ is the overall change in steady state friction coefficient and $\Delta \ln V$ is a step change in sliding velocity (Marone, 1998). The values are typically determined by performing velocity stepping experiments. The sliding velocity is instantaneously increased or decreased when a steady state friction situation is reached. The difference in the steady state friction before and after the change is expressed as the parameter *(a-b)*. A positive value in *(a-b)* i.e. > 0 indicates an increase in steady state friction coefficient ($\Delta \mu_{ss}$) and can be considered as velocity strengthening (i.e. stable frictional slip). A negative value in *(a-b)* i.e. <0 indicates a decrease in steady state friction coefficient ($\Delta \mu_{ss}$) and can be considered to be velocity weakening (i.e. potentially unstable stick-slip) (Scholz, 1998). Data for the velocity dependence of friction is constructed by modeling the constitutive parameters, *a, b* and *Dc* for each velocity step. Friction is modeled by using two state variables b_1 and b_2, associated with two critical slip distances D_{c1} and D_{c2}, or only one state variable, b (see Figure 2).

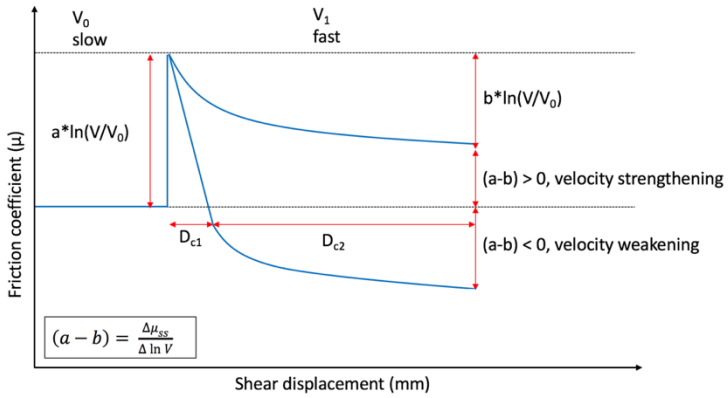

Figure 2: Rate and state dependent friction model, illustrating a step change in velocity, V_0 to V_1. The parameter *(a-b)* is the difference in the steady state friction before and after the velocity change. A positive *(a-b)* >0 indicates an increase in steady state friction coefficient ($\Delta\mu_{ss}$), i.e. velocity strengthening. A negative value in *(a-b)* <0 indicates a decrease in steady state friction coefficient ($\Delta\mu_{ss}$), i.e. velocity weakening.

3. Materials and methods

3.1 Sample material

In this report, clay samples with varying mineral compositions and contents of hematite are used in friction experiments using a ring shear apparatus: 1) pure illite with varying hematite content, and 2) hematite-bearing clay-rich rock from a natural CO_2 field (the Carmel formation). X-Ray Diffraction (XRD) analysis as well as Inductively Coupled Plasma (ICP) mass spectrometry was performed on all samples and results were combined to constrain element composition and the bulk mineralogy. The XRD analysis was done on bulk samples, while for the ICP mass spectrometry the sample was dissolved in a fluid.

The first set of samples of pure illite were obtained from De Kruiderie. The clays are mined in the Provence, the South of France, where they are dried and crushed to fine powder (Salts Clay Minerals, n.d.). This first set of samples consist of a white illite clay, a green illite clay and a red illite clay and were provided in powdered form (Figure 3a, b and c). Sample description suggested that these samples were mostly illite-clays, but XRD and ICP analyses showed that considerable amounts of different minerals were present (see section 3.2). Grain size analysis of the white illite clay and the red illite clay was performed twice using a Malvern laser particle sizer to determine the grain size distribution of the sample. In addition, extra natural quartz powder (Min-u-Sil 15) is added to the white illite clay to analyze the effect of quartz on the frictional strength. An amount of ~0,63 gram of quartz is added to ~1 gram of white illite powder, to obtain a quartz content of ~40%.

The second sample is a sample derived from the CO2W55 core from a natural CO_2 complex near Green River, Utah (USA) obtained in a drilling campaign in July, 2012. The sample was derived from a ~322 m deep vertical hole, drilled through a CO_2-charged sandstone reservoir as well as their intervening caprocks (Kampman, et al., 2014). The caprock used for this study is part of the 65-90 m thick Carmel Formation of Jurassic age. The Carmel formation lies on top of the CO_2-

charged Navajo Sandstone and is overlain by the CO_2-charged Entrada Sandstone. The Carmel Formation consists of marine sediments containing red and grey shale, red and grey claystone/siltstone and fine grained sandstone (Kampman, et al., 2013). A sample (CCV-70A) from the Carmel Formation was used for this study (Figure 3e). The CCV-70A sample from the Carmel Formation sample was crushed and sieved to a grain size below 125 μm. XRD results from a sample 30 cm lower in the formation showed that the sample (sample CCH-4, depth: 492,7) contained: 38.9% Quartz, 27.7% Illite, 18.2% Dolomite, 9.1% K-feldspar, 2.5% Albite, 2.3% Calcite and 1.4% Hematite.

Figure 3: Sample material used in this study in powder form. (a) white illite clay, (b) red illite clay, (c) green illite clay, (d) red illite clay processed with sodium dithionite (hematite is dissolved), (e) Carmel CCV-70A sample, (f) ring shaped pressed sample with an inner diameter of 22 mm, an outer diameter of 28 mm and thickness of ~1 mm.

3.1.1 Removing hematite - Sodium dithionite procedure

To simulate the bleaching related to CO_2 penetration in the red clay sample and the Carmel CCV-70A sample, a sodium dithionite ($Na_2S_2O_4$) bleaching procedure was performed to dissolve the hematite (i.e. the cause of the red color) from the samples. In order to dissolve the hematite from the sample, about 6.5 grams of sample material was brought into suspension with 400 ml of distilled water using a magnetic stirrer at a temperature of 50°C after which 50 ml of a 10% dissolved $Na_2S_2O_4$ solution (10 grams in 100ml of distilled water) was added to the suspension in order to dissolve the hematite. The procedure was performed successfully if the red color had disappeared from the suspension. After the procedure was performed and the suspension was

settled, most of the liquid was poured off. The sample material was washed several times with distilled water. To accelerate the precipitation-process each time, a laboratory Heraeus Sepatech, Megafuge 1.0 Centrifuge was used for approximately 10 minutes at ~1000-1500 rpm, after which the water was poured off again. In the end, the suspension was dried and sieved to powder form again (Figure 3d). The procedure was done for both the red illite powder as well as the Carmel formation powder. Figure 4 shows the set-up of the procedure as well as the results of the dissolved color after ~1 hour.

a b

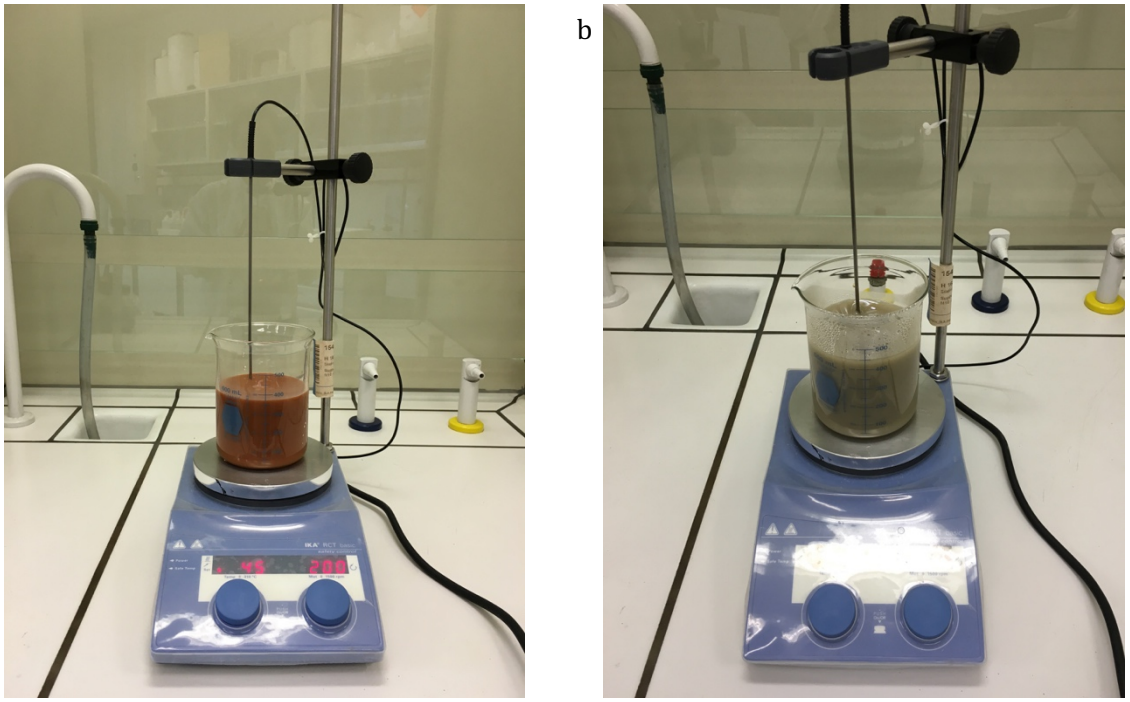

Figure 4: Sodium dithionite procedure using a magnetic stirrer at a temperature of 50°C, (a) Suspension of 6.5 grams of red illite sample material with 400 ml of distilled water, (b) after ~1h of adding the sodium dithionite dissolution to the suspension and the red color has disappeared from the suspension.

3.2 Sample analysis

The mineralogical bulk composition derived from ICP and XRD analysis and grain size properties of the samples will be shortly described for the samples used in this study.

3.2.1 Grain size analysis

The grain size analysis of the red and white illite is performed twice to have an approximation of the grain size. Results of the grain size analysis (median diameter, d_{50}) showed that the grain size of the red illite is approximately d_{50}= ~4.45 – 5.24 μm (RI1 = 4.45 μm and RI2 = 5.24 μm), and the white illite has a grain size approximately d_{50}= ~11.34 – 11.45 μm (WI1 = 11.34 μm and WI2 = 11.45 μm). The average grain size is calculated as d = 7.51 μm (RI1), d = 9.00 μm (RI2), d =13.8 μm (WI1) and d = 13.9 μm (WI2). The grain size distribution is shown in Figure 5. The shape of

the distribution is lognormal. The grain size analysis of the white illite samples shows a perfect reproducibility as both of the analysis show the same distribution. The analyses of the red illite also shows a good reproducibility, but the distribution is a bit more divided.

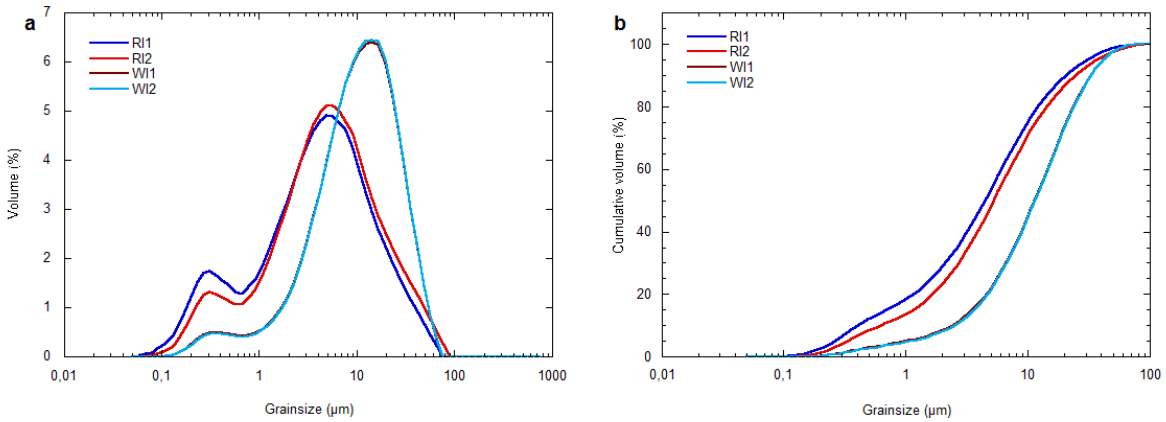

Figure 5: (a) Grainsize distribution for the red illite (RI1 and RI2) and white illite (WI1 and WI2) performed twice with a laser particle sizer, (b) grain size distribution in cumulative volume %.

3.2.2 XRD and ICP analysis

The results of the X-Ray diffraction (XRD) analyses and Inductively Coupled Plasma (ICP) mass spectrometry analysis are listed in Table 1 and Table 2, respectively. Sample description suggested that these samples were mostly illite-clays. The values of the ICP and XRD analysis are combined to obtain an average calculated composition of the samples and are listed in Table 3. Since the grain size of the clay minerals is generally small (< 10 µm) and the structure diverse, it makes it difficult for XRD analysis to distinguish individual peaks for clay minerals. Usually, in XRD, if broad peaks are present, it is likely that clay minerals are present, but identifying the individual clay minerals is harder since their peaks are all closely spaced in the XRD pattern (Moore D. , 1997). Therefore, the results of the XRD are only used for identifying the type of minerals present and the quantity of the minerals is calculated by using ICP results.

XRD analysis showed a composition of the red illite consisting of quartz, illite, kaolinite, phengite and hematite, whereas the white illite consists of mainly illite, microcline and quartz, the green illite consists of phengite, illite, quartz, kaolinite and microcline. The red illite sample material used for the sodium dithionite procedure showed that indeed all the hematite was dissolved, since the sample only consist of quartz, phengite, kaolinite and talc. The XRD analysis of the Carmel CCV-70A sample showed that the sample consists of mainly microcline, phengite, dolomite and quartz, and some albite, calcite and goethite are present. The results from the ICP analysis showed that all samples were mainly rich in Al, Si, K, Na and Fe (values are given in ppm (mg/kg)).

Sample material	XRD mineralogy
Red illite	quartz, illite, phengite, kaolinite, hematite
White illite	dickite, microcline, quartz, illite (vivianite)
Green illite	illite, quartz, phengite, kaolinite, microcline, calcite
Red illite w/o hematite	quartz, phengite (illite), kaolinite, talc
Carmel CCV-70A	quartz, microcline, dolomite, albite, phengite, calcite, goethite

Table 1: Mineralogy results for the 5 samples based on X-Ray Diffraction (XRD). Minerals are listed on approximate quantity from most to least present in the sample.

Sample name	Red Illite	White Illite	Green Illite	Red Illite w/o hematite	Carmel CCV-70A
Element - wavelength	ppm (mg/kg)	ppm (mg/kg)	ppm (mg/kg)	ppm (mg/kg)	ppm (mg/kg)
Al 394.401	93928,770	156506,840	79326,680	98406,930	35426,800
Ba 455.404	552,250	888,710	288,850	506,760	283,430
Be 313.107	*15,470*	*14,600*	*14,810*	*16,960*	*11,700*
Ca 315.887	-	-	26639,560	-	39483,820
Ca 396.847	2714,950	462,080	-	836,560	-
Co 230.786	< dl	< dl	< dl	< dl	< dl
Cr 205.618	121,620	*43,830*	119,620	127,570	*46,820*
Cu 324.754	< dl	*121,420*	< dl	< dl	< dl
Fe 259.941	44026,890	2471,900	32130,010	18625,920	12362,640
K 766.491	22421,420	21701,720	21681,050	23925,160	27233,870
Mg 285.213	4528,970	481,310	11367,200	4316,860	15829,140
Mn 257.611	352,980	< dl	378,080	63,900	351,530
Mn 260.569	368,510	*36,380*	391,100	93,040	364,310
Mo 202.095	< dl	< dl	< dl	< dl	< dl
Na 589.592	4788,800	4718,340	4012,820	5189,770	6403,330
Ni 231.604	< dl	< dl	< dl	< dl	< dl
P 177.495	292,480	762,350	< dl	*252,750*	322,620
Pb 220.353	< dl	986,690	< dl	< dl	< dl
S 182.034	< dl	< dl	< dl	< dl	< dl
Sc 424.683	*14,930*	< dl	*11,640*	*16,010*	< dl
Si 251.612	278240,920	228530,480	251827,390	299767,840	308248,150
Sr 407.771	113,240	136,320	39,090	108,620	103,560
Ti 334.187	5446,900	2136,530	3719,410	5835,340	2086,210
V 292.402	195,580	*59,150*	*89,700*	205,590	*73,430*
Y 324.228	*48,000*	*23,800*	*33,760*	*48,010*	*23,060*
Zn 206.200	98,430	*38,250*	95,460	82,760	46,060
Zr 343.823	234,530	*61,350*	*162,310*	*218,920*	244,200

Table 2: Results of the Inductively Coupled Plasma (ICP) Mass Spectrometry analysis for 5 samples, values are given in ppm* (mg/kg).

*Note, values less than the detection limits are given with a "<" symbol. Values below the *Background Equivalent Concentration* (BEC) are marked *italic* and can have an error of > 10% and are seen as an approximate value. The BEC value is the concentration of an element which would produce the same emission intensity as the plasma background measured at the analyte wavelength.

Both analyses combined resulted in a quantitative mineralogical composition listed in Table 3. The illite content ranges between 15% - 38%, with the white illite and green illite having the lowest illite content and the red illite the highest illite content. The quartz content ranges between 1.5% - 20%, with the Carmel CCV-70A sample having the highest quartz content (~20%) and the white illite having the lowest quartz content (~1.5%). Depending on the amount of potassium in illite and microcline, the contents in the white and green illite can vary significantly, as showed in Table 3 as option 1, 2 and 3. Option 1 shows the mineral composition when all potassium is in illite, option 2 all potassium in microcline and option 3 shows the minerals composition when potassium is divided equally (50/50).

Furthermore, other phyllosilicate clay minerals are present, e.g. kaolinite (17% – 40% in red illite and green illite) and dickite (~75% in white illite) and phyllosilicate mica minerals like phengite (11% - 38%). Hematite is only present in the red illite sample and the Carmel CCV-70A sample with contents of 2.9% and 1.3%, respectively.

Mineral	**Chemical formula**	**Red Illite**	**RI w/o hematite**	**Carmel CCV-70A**	**White illite**			**Green illite**		
					Option 1	*Option 2*	*Option 3*	*Option 1*	*Option 2*	*Option 3*
Quartz	SiO_2	7.79%	9.829%	20.722%	1.41%	1.68%	1.53%	11.38%	13.88%	12.51%
Illite	$KAl_2(Si_4O_{10})(OH)_2$	36.35%	37.882%	-	28.95%	0.00%	15.75%	28.30%	0.00%	15.55%
Kaolinite	$Al_2Si_2O_5(OH)_4$	39.85%	40.195%	-	-	-	-	21.21%	35.12%	27.48%
Hematite	Fe_2O_3	2.91%	-	1.269%	-	-	-	-	-	-
Phengite	$K(AlMg)_2(OH)_2(SiAl)_4O_{10}$	12.95%	11.806%	14.608%	-	-	-	35.07%	42.77%	38.54%
Dolomite	$CaMg(CO_3)_2$	-	-	13.662%	-	-	-	-	-	-
Microcline	$KAlSi_3O_8$	-	-	32.642%	0.00%	15.28%	6.97%	0.00%	3.30%	1.49%
Calcite	$CaCO_3$	-	-	3.393%	-	-	-	3.59%	4.38%	3.94%
Dickite	$Al_2Si_2O_5(OH)_4$	-	-	-	69.55%	82.94%	75.66%	-	-	-
Albite	$NaAlSi_3O_8$	-	-	13.639%	-	-	-	-	-	-
Left over	-	0.14%	0.285%	0.0610%	0.09%	0.10%	0.09%	0.45%	0.55%	0.49%
Total	-	100%	100%	100%	100%	100%	100%	100%	100%	100%

Table 3: Mineral composition of each sample based on X-Ray Diffraction (XRD) analysis and Inductively Coupled Plasma (ICP) mass spectrometry analysis. (Option 1: all potassium in illite, 2: all potassium in microcline, 3: potassium divided equally (50/50) over illite and microcline)

3.3 Sample preparation

To prepare a sample for testing in the ring shear apparatus all the powder sample materials were pressed in a ring-shaped sample with an inner diameter of 22 mm and an outer diameter of 28 mm (Figure 3f). For the pre-pressing about ~0.53 g of sample material and about ~0.04 g of distilled water was used for each sample. The sample material was then pressed in a specially designed device at 170 MPa for 20 minutes in the presence of water vapor at room temperature to end up with a ring-shaped sample of roughly 1 mm thick. The sample was dried overnight in an

oven at 50 °C to determine the final weight of the ring. Table 4 shows the measured properties, like the final weight, dimensions, mineral composition and porosity for each sample used in the experiments. The porosity is determined by assuming the density of the illite clay samples to be ~2.63 - 2.76 g/cm^3 (see Table 4) depending on their mineral composition as listed in Table 3, which results in starting porosities of about 13% - 17% for the illite samples and 17% for the Carmel samples, respectively.

Experiment	Sample name	Thickness ring (mm)	Volume sample (mm^3)	Weight sample (g)	Weight water (g)	Weight ring (g)	Density (g/mm^3)	Porosity (%)
u416_WI2035TR	White illite	1.10	259.1814	0.56051	0.03527	0.53303	0.00263	17.771
u418_RI2035TR	Red illite	1.05	247.4004	0.56083	0.03527	0.51917	0.00276	17.866
u422_GI2035TR	Green illite	1.00	235.6194	0.56086	0.03615	0.47341	0.00268	11.180
u425_WIQ2035TR	White illite + quartz	1.10	259.1814	0.56165	0.03752	0.49952	0.00265	18.226
u427_RI2_2035TR	Red illite	1.00	235.6194	0.56134	0.03527	0.50024	0.00276	13.681
u428_WI2_2035TR	White illite	1.10	259.1814	0.56107	0.03587	0.50656	0.00263	17.689
u432_RI3_2050TR	Red illite	1.05	247.4004	0.56116	0.03674	0.48642	0.00276	17.818
u433_WI3_2050TR	White illite	1.10	259.1814	0.57184	0.03664	0.52123	0.00263	16.109
u436_RI4_2050T120	Red illite	1.00	235.6194	0.56124	0.03692	0.48243	0.00276	13.697
u438_RI5_2050T200	Red illite	1.00	235.6194	0.56099	0.0366	0.51497	0.00276	13.735
u439_RI6_5020TR	Red illite	1.00	235.6194	0.5615	0.03617	0.49842	0.00276	13.657
u441_IWH_2050TR	Illite w/o hematite	1.00	235.6194	0.56203	0.03587	0.51026	0.00276	13.575
u445_IWH2_5020TR	Illite w/o hematite	1.05	247.4004	0.57034	0.04226	0.53159	0.00276	16.473
u447_RI7_2050T200	Red illite	1.05	247.4004	0.57164	0.03624	0.51567	0.00276	16.283
u448_CCV70A_TR	Carmel	1.10	259.1814	0.5609	0.03602	0.5474	0.00268	19.249
u450_CCV70AWH_TR	Carmel w/o hematite	1.10	259.1814	0.56204	0.03604	0.48537	0.00269	19.386

Table 4: List of experiment names, sample material used, initial thickness and volumes of the pressed rings, initial weight of the sample material and pressed ring, calculated density for corresponding sample material and the calculated porosity for each sample.

3.4 Experimental apparatus and procedure

The frictional sliding experiments were performed using a hydrothermal ring shear machine in the High Pressure and Temperature Laboratory at the Utrecht University, which is described in detail by Niemeijer et al., 2008 (Figure 6a). In this machine, a ring shaped sample (thickness ~1mm, Figure 3f) is held between two roughened nickel super alloy, René 41, pistons and kept in place between an inner (22 mm diameter) and outer (28 mm diameter) confining ring (Figure 6c). The confining rings were coated with a D321R Molykote Anti Friction coating to reduce wall friction (Figure 6d). The initial length of the piston-sample assembly was measured before and after the experiment, to determine the difference in sample thickness and amount of layer thinning. Layer thinning could occur during an experiment due to compaction of the sample by

the application of normal load or by the loss of sample material which squeezed out between tiny gaps between the confining rings and the pistons. Normal load was applied via a pressure-compensated upper loading piston and is measured externally (± 0.05 kN) using a 100 kN Instron load cell. A servo-controlled motor and gearbox system controls the rotation of the vessel and internal lower piston together in the Instron loading frame so that the entire vessel rotates with respect to the upper piston, shearing velocities of 0.010 to 300 μm/s can be produced. The rotation of the lower piston generates a shear displacement on the ring-shaped sample, which results in a shear stress. The shear stress and torque (± 6 Nm) generated are measured externally using a couple of load cells with a full scale of 1.2 kN each, located in a cross-bar. Displacement of the Instron ram was measured using a linear variable differential transformer (LVDT) with a full scale of 100 mm.

To perform an experiment, the piston-sample assembly was installed into the internally heated pressure vessel and sealed using an upper closure nut. Sample temperature was measured with a thermo couple close to the sample layer (± 1°C). The whole vessel was positioned into a servo-controlled Instron loading frame. After the vessel was positioned correctly, normal stress was applied and the pressure vessel was manually filled with demineralized water, which formed the pore fluid for the experiment (Niemeijer et al., 2008). In experiments at elevated temperatures, the pore fluid was pressurized in the vessel first before heating, since the heating will cause the pore fluid pressure to increase rapidly. After the temperature was settled, the pore fluid pressure was adjusted manually to the desired value. The system was left to equilibrate for ~0.5-1.0 hour, before the experiment was initiated by switching on the rotary drive systems and started with the programmed conditions for the experiment.

Three types of ring shear experiments were performed for this study: (1) velocity stepping experiments with constant applied effective normal stress (σ_n^{eff}) of 20, 27.5 and 35 MPa respectively, (2) normal stress stepping experiments at constant sliding velocity of 1 μm/s, and (3) a combination of both normal stress stepping experiments as well as velocity stepping experiments.

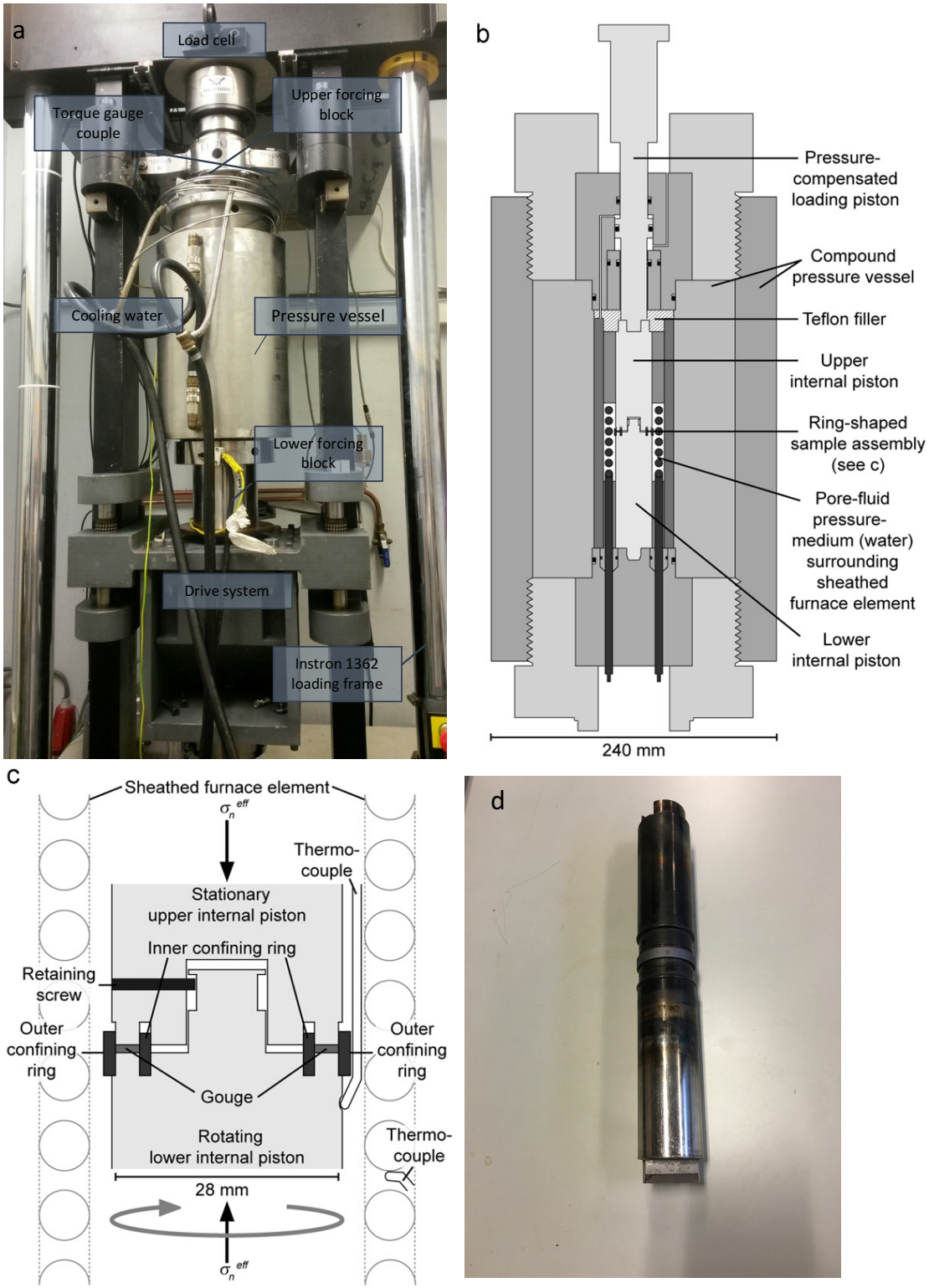

Figure 6: (a) photograph of the hydrothermal ring shear apparatus and pressure vessel loaded inside of the Instron loading frame used in this study, (b) schematic overview of the pressure vessel (image after Den Hartog et al., 2013), (c) schematic overview of the sample assembly (image after Den Hartog et al., 2013), (d) piston set, including the confining rings (piston set HT2).

3.4.1 Velocity stepping experiments

All experiments performed in this section were velocity stepping tests, using sliding velocities (*v*) of 1, 3, 10, 30 and 100 μm/s and displacements of 0.6, 0.6, 0.9, 0.9, 0.9 mm respectively for three values of applied normal stresses during the experiment. The experiments were performed on the illite sample set, including the white illite, red illite, green illite and white illite with quartz. First, an applied normal stress (σ_n^{eff}) of 20 MPa was used with an initial run-in sliding velocity of 10 μm/s for a displacement of 1 mm after which the velocity stepping sequence was performed twice. Next, the applied normal load was increased to 27.5 MPa followed by 35 MPa both with an initial run-in sliding velocity of 10 μm/s for 0.5 mm displacement, after which the velocity stepping was performed twice again. All the experiments were performed at room temperature, using a fluid pressure (P_f) of 15 MPa to simulate in-situ reservoir conditions, at least in terms of stress and fluid pressure. The performed velocity stepping experiments are listed in Table 5 as experiment number U416 – U428.

3.4.2 Normal load stepping experiments

These experiments were performed on the illite sample set (i.e. red illite, white illite and red illite w/o hematite) at a constant sliding velocity (*v*) of 1 μm/s and an initial run in of 2 mm displacement. An initial normal stress of 20 MPa was applied during the run in period of 2 mm displacement followed by normal load stepping. The normal load stepping was applied quasi-instantaneously by changing the normal load with steps of 3 MPa in 10 seconds during sliding. The next σ_n^{eff}-step was performed when steady state was reached after approximately ~0.5 mm of displacement. The normal load was either started at 20 MPa and increased to 50 MPa (load up) with steps of 3 MPa and stepped down again to 20 MPa (load down), or started at 50 MPa, decreased to 20 MPa with steps of 3 MPa and stepped up to 50 MPa. In all of the experiments the pore fluid was held constant at 15 MPa and the temperature was constant at room temperature, 120 °C or 200 °C. The conditions at which the experiments were performed are listed in Table 5 under experiment numbers U432 – U447.

3.4.3 Normal load and velocity stepping experiments

This set of experiments was performed on the samples of the Carmel Formation and was performed with both steps in σ_n^{eff} as well as velocity steps. An initial shear displacement of ~2 mm was carried out at constant velocity and effective normal stress of 20 MPa before the velocity and normal load stepping was performed. For every normal load step a set of velocity steps was performed at 1, 10 and 100 μm/s with a displacement of 0.6, 0.9 and 0.9 mm respectively. With a starting σ_n^{eff} of 20 MPa, the σ_n^{eff} was increased up to 50 MPa with steps of 5 MPa and decreased

back to 20MPa with steps of 5 MPa. In both the experiments the pore fluid was held constant at 15 MPa and the temperature was constant at room temperature. The conditions at which the experiments were performed are listed in Table 5 under experiment numbers U448 and U450.

3.5 Data processing

Shear displacement, axial displacement, normal force, torque, temperature (± 1 °C) and pore fluid (±0.005 MPa) were logged as voltage signals measured externally using a 16-bit A/D converter and a logging frequency of 1 – 100 Hz depending on the sliding velocity. The externally measured torque and normal force data was corrected for seal friction. For all experiments, the apparent coefficient of friction (μ_a) was measured directly during the experiment by the ratio of shear stress to the normal stress; $\mu_a = \tau/\sigma_n$. However, for each normal load stepping experiment, the recorded normal stress and shear stress was used to determine the dependence of shear stress (τ) on the effective normal stress (σ_n^{eff}) applied, since $\tau = S_0 + \mu\sigma_n^{eff}$. A linear relation between shear stress and effective normal stress was plotted to obtain values for the cohesion S_0 and the internal coefficient of friction (μ_{int}).

The velocity dependence of friction (μ) is quantified in a rate and state-dependent friction model using the *(a-b)* parameter (equation 2). In case of steady state, when $\frac{d\theta}{dt} = 0$, the (a-b) parameter gives: $(a-b) = \frac{\Delta\mu_{ss}}{\Delta \ln V}$. In general, the *(a-b)* values were determined by inverting the Dieterich-type RSF equation (eq. 2 given in section 2.2) coupled to eq. 4 describing the elastic interaction between the sample and the loading frame for the constitutive parameters *a, b,* and slip distance d_c using an iterative least-squares fitting method (Reinen & Weeks, 1993).

$$\frac{d\mu}{dt} = K(V_{lp} - V) \tag{4}$$

in which K = is the apparatus stiffness normalized by normal stress, V_{lp} = load point velocity, V= sliding velocity (Reinen & Weeks, 1993). Data is de-trended as described by Tembe et al., 2010, for the μ versus displacement curves for calculating *(a-b)* to remove background hardening or weakening trends.

Experiment	Sample name	σ_n (MPa)	T (°C)	Pf (MPa)	V (µm/s)	Final thickness (mm)	Final shear *d* (mm)
u416_WI2035TR	White illite	20, 27.5, 30	Room	15	1-3-10-30-100	0.45	43.4
u418_RI2035TR	Red illite	20, 27.5, 30	Room	15	1-3-10-30-100	0.95	43.4
u422_GI2035TR	Green illite	20, 27.5, 30	Room	15	1-3-10-30-100	0.49	43.4
u425_WIQ2035TR	White illite + quartz	20, 27.5, 30	Room	15	1-3-10-30-100	1.18	43.4
u427_RI2_2035TR	Red illite	20, 27.5, 30	Room	15	1-3-10-30-100	0.30	48.4
u428_WI2_2035TR	White illite	20, 27.5, 30	Room	15	1-3-10-30-100	0.93	43.4
u432_RI3_2050TR	Red illite	20 – 50 – 20	Room	15	1	0.93	12.5
u433_WI3_2050TR	White illite	20 – 50 – 20	Room	15	1	1.21	12
u436_RI4_2050T120	Red illite	20 – 50 – 20	120	15	1	0.42	12.5
u438_RI5_2050T200	Red illite	20 – 50 – 20	200	15	1	1.16	12.5
u439_RI6_5020TR	Red illite	50 – 20 – 50	Room	15	1	0.14	11
u441_IWH_2050TR	Illite w/o hematite	20 – 50 – 20	Room	15	1	1.20	12.5
u445_IWH2_5020TR	Illite w/o hematite	50 – 20 – 50	Room	15	1	0.97	12.5
u447_RI7_2050T200	Red illite	20 – 50 – 20	200	15	1	1.36	12.5
u448_CCV70A_TR	Carmel CCV-70A	20, 25, 30, 35, 40, 45, 50	Room	15	1-10-100	0.72	33.2
u450_CCV70AWH_TR	Carmel WH CCV-70A	20, 25, 30, 35, 40, 45, 50	Room	15	1-10-100	0.65	33.2

Table 5: List of experiment numbers, sample material and corresponding conditions at which the experiments are performed. (σ_n = applied normal stress; T = temperature (°C); Pf = pore fluid pressure (MPa); V = sliding velocity (µm/s); final sample thickness in mm; *d* = final shear displacement (mm)).

4. Results

4.1 Mechanical Data

A list of the performed experiments is provided in Table 5, including the experimental conditions such as normal load applied, temperature, sliding velocity, sample thickness and final shear displacement. First, the results of the velocity stepping experiments will be described, followed by the normal stepping experiments, the Carmel experiments and the velocity dependence of friction for all the experiments.

4.1.1 Velocity stepping experiments

The friction coefficient (μ) versus displacement plots are illustrated in Figure 7a, for the experiments performed on the white illite (u416), red illite (u418), green illite (u422) and white illite with extra quartz powder added (u425). Figure 7b shows the friction coefficient versus displacement curves for the white illite (u416 and u428) and red illite samples (u418 and u427) repeat experiments performed at room temperature, effective normal stress of 20, 27.5 and 35 MPa and fluid pressure of 15 MPa. The total shear displacement for the experiments was ~43.4 mm. All experiments show a rapid increase in μ after the start of the experiment, followed by a run in period of ~1 mm displacement at which μ stabilized and reached steady state. For the green illite and red illite μ increased steadily during the run in period while for the white illite and white illite with quartz there was a peak in μ followed by a weakening. After the run in period the velocity steps were applied for each effective normal stress. For all these experiments, the velocity steps were increased from 1 to 3, 10, 30 and 100 μm/s. When the next effective normal stress step is applied, μ typically decreases and again steady state was obtained during a run in period of ~0.5 mm. During the velocity steps, a hardening trend can be observed for all experiments, including the repeat experiments. The friction coefficient increases with each velocity step. In Figure 7, it is shown that the red illite sample exhibits the highest apparent friction (μ_a) varying between μ_a = ~0.30 – 0.46, followed by the white illite with extra quartz with μ_a = ~0.30 – 0.40. The white illite and green illite shows almost similar curves for the friction coefficient (μ_a = ~0.20 – 0.35). Overall, all samples show relatively low coefficient of friction, i.e. lower than those predicted by Byerlee's rule, which is typical for clay samples (see section 2.1). The repeat experiments performed for the red illite do not show a good reproducibility of the results, since both experiments show different evolutions of the friction coefficient. The u427 experiment shows a decrease in friction coefficient during the run-in period while the u418 experiment shows an increase in μ during the run-in period. In addition, μ is much lower in the u427 experiment for the red illite than μ in the first

(u418) experiment. The repeat experiment for the white illite (u428) does show results which are quite similar and show the same trends as u416.

Figure 8 shows the linear relation between the shear stress and the effective normal stress for the velocity stepping experiments. In all experiments, shear stress increases with effective normal stress, which is used to calculate the coefficient of friction, by fitting a straight line through the data points using the least-squares methods. The straight line fits the data points plotted for the shear stress at each effective normal stress with the relationship $\tau = \mu\sigma_n^{eff} + S_0$, the corresponding data is listed in Table 6. In Table 6, values are obtained for the friction coefficient (μ) as the slope of the line and the cohesion (S_0) as the constant in the formula for each experiment. The results are quite different, comparing the individual experiments. The difference can also be obtained from the figure, which shows various slopes and values of shear stress. Values for μ vary between μ_{int} = ~0.207 for the white illite experiment and μ_{int} = ~0.5467 for the red illite experiment. The red illite and white illite with extra quartz show the highest plotted values for shear stress in Figure 8. Again, the repeat experiments are not showing a good reproducibility of the results, since the results for the friction coefficient are varying quite much, i.e. between μ_{int} = 0.207 and μ_{int} = 0.5467, which is a difference of ~0.3 comparing the individual experiments. No good relationship can be observed between the friction coefficient and the different sample materials.

The cohesion value (S_0) does not show a systematic trend either, and for some experiments even a negative value of cohesion is obtained, which in theory, does not exist. In particular, the experiment performed on the red illite 2 (u427), white illite 2 (u428) and the white illite with quartz (u425) show unrealistic high negative values. Especially the high negative value (S_0 = -8.02) of the red illite 2 experiment (u428 repeat experiment) is therefore considered not representative compared with the first red illite experiment. Since the straight line is based on only 3 data point for each experiment, the correlation coefficient (R^2) does not show a perfect fit in some cases (R^2=0.77), which can also be observed in Figure 8.

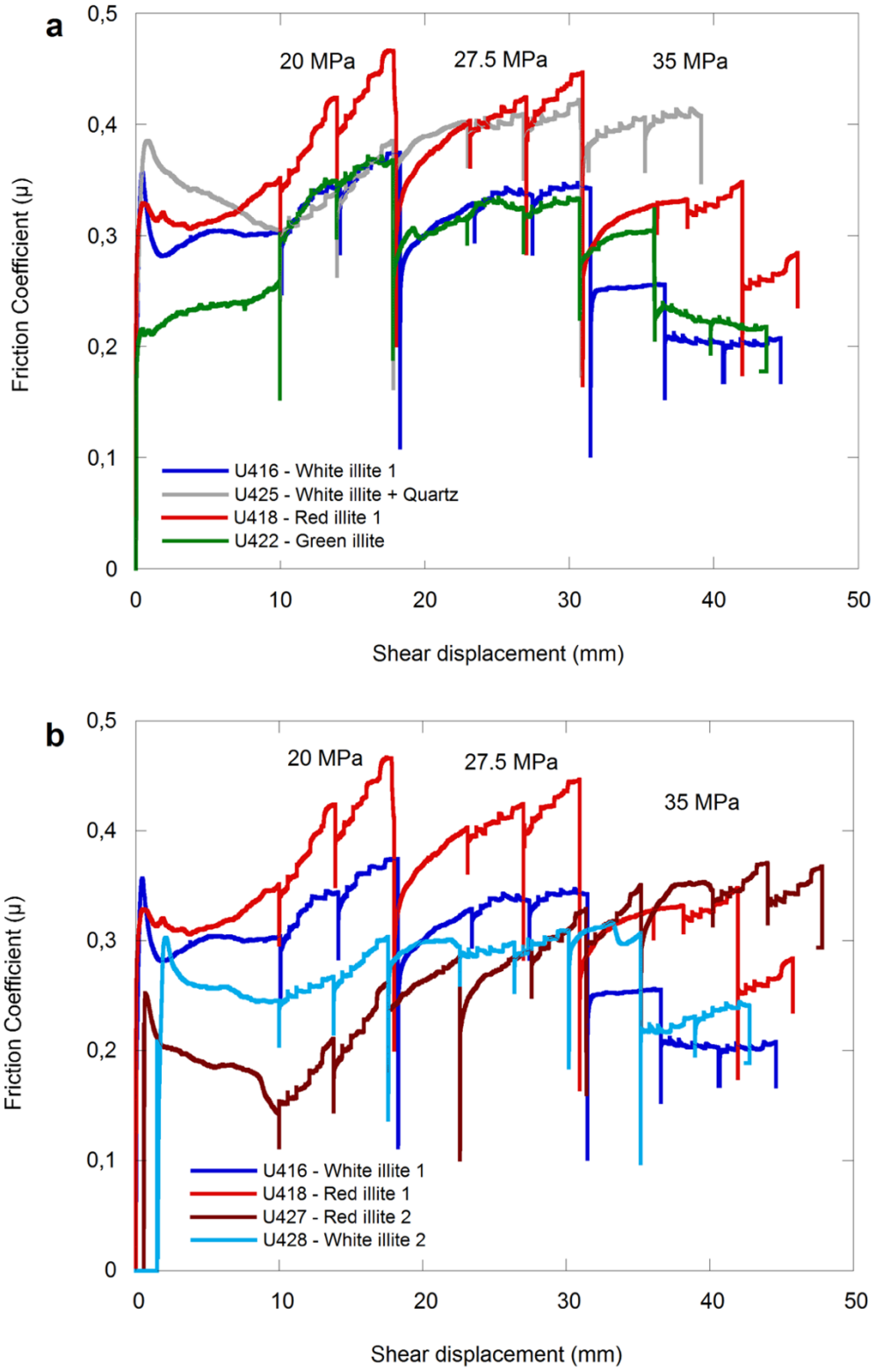

Figure 7: Evolution of the friction coefficient with shear displacement for the velocity stepping experiments, (a) experiment u416, u418, u422 and u425 and for (b) repeat experiment for the white illites (u416 and u428) and red illite samples (u418 and u427) at room temperature, effective normal stress of 20, 27.5 and 35 MPa, respectively and fluid pressure of 15MPa.

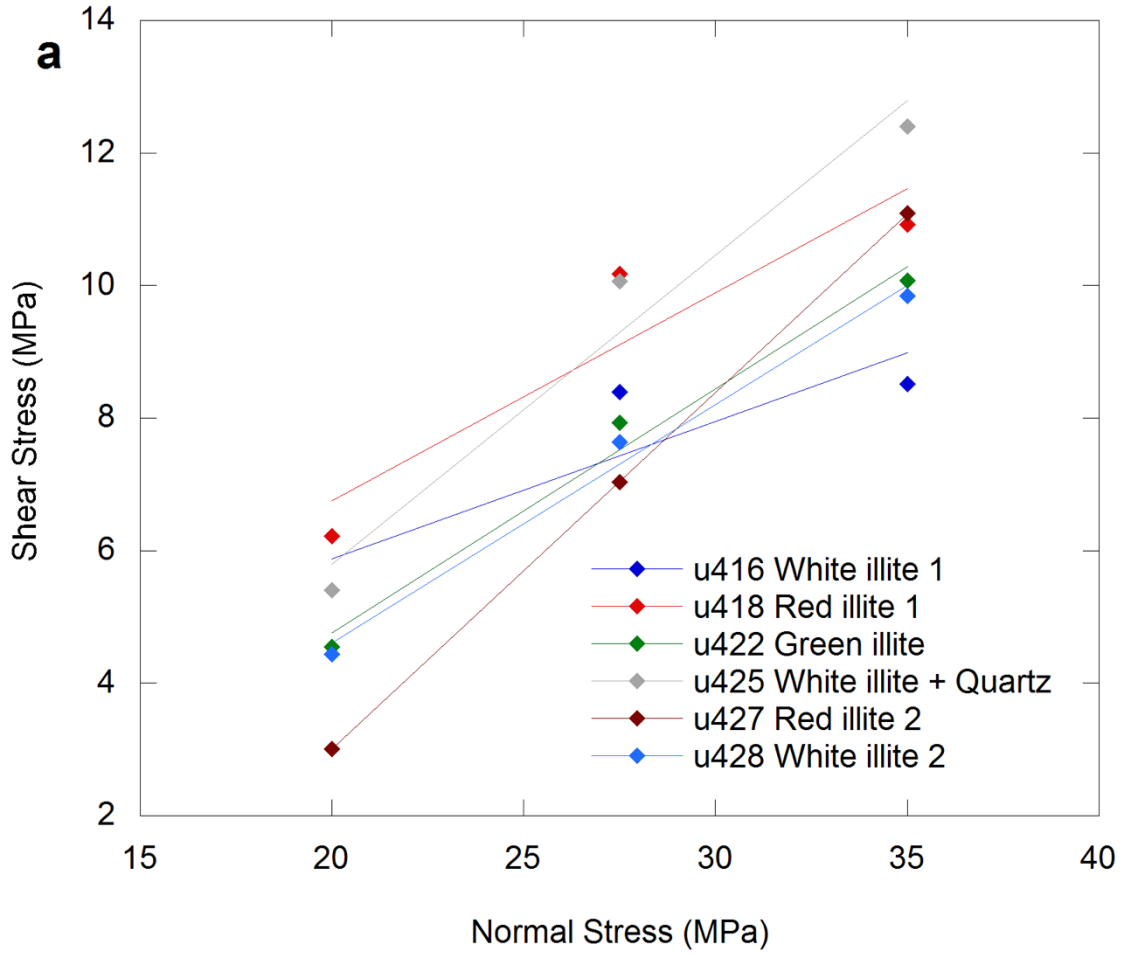

Figure 8: Shear stress vs. effective normal stress for the velocity steps experiments (u416 – u428). Shear stress values are plotted at steady state. Lines are straight line fit $\boldsymbol{\tau = S_0 + \mu\sigma_n^{eff}}$. Friction coefficients (slopes) are listed in Table 6.

Experiment	Sample name	Straight line fit $\tau = \mu\sigma_n^{eff} + S_0$	R^2
u416	White Illite	y = 0,207x + 1.744	0,7777
u418	Red Illite	y = 0,3138x + 0.476	0,8654
u422	Green Illite	y = 0.3681x – 2.6002	0,9834
u425	White Illite + Quartz	y = 0,4663x – 3.5287	0,9643
u427	Red Illite 2	y = 0,5467x – 8.0294	0,9999
u428	White Illite 2	y = 0,3779x – 2.9964	0,9946

Table 6: List of the linear relations between shear stress and effective normal stress for the velocity stepping experiments, showing the slope of the line as friction coefficient ($\boldsymbol{\mu}$) and the cohesion S_0. (σ_n = applied normal stress in MPa; T = temperature in °C; R^2= correlation coefficient).

4.1.2 Normal load stepping experiments

In Figure 9 the evolution of the friction coefficient (μ) with displacement is shown for the normal load stepping experiments performed on the red illite (u432, u436, u438, u439 and u447), white illite (u433) and illite without hematite (u441 and u445) performed at room temperature, 120°C and 200°C, at effective normal stresses of 20 – 50 MPa with a constant sliding velocity of 1 μm/s. Normal load stepping is performed with steps of 3 MPa for each experiment. Experiment conditions are listed in Table 5 for each experiment. Figure 9 shows the μ versus displacement curves for all the normal load stepping experiments, which show mostly similar results. All the experiments show a rapid increase in friction after the start of the experiment, followed by a stabilization of the friction coefficient with a run in period of ~2 mm at which the friction coefficient slightly decreases and stabilizes. The total shear displacement for the experiments was ~12 mm. For the experiments at which the normal load increases from 20 MPa to 50 MPa, μ typically decreases initially after the extra 3 MPa of normal load is applied, while μ typically increases initially after the normal load is decreased with 3 MPa. In both cases, μ reached steady state after about ~0.5 mm for each normal load step. In Figure 9a, it can be observed that the apparent friction coefficient (μ) lies between values of μ_a = ~0.22 – 0.30 at least for the first set of normal load stepping. For the second part of the experiment the evolution of μ deviates from the trend observed in the first part of the experiment. In experiment u433, u436 and u438 a hardening trend can be observed while for experiment u432, u439, u441, u445 and u447 a weakening trend can be observed. There is no clear correlation between the weakening/hardening trends and the applied normal load and temperature, since the experiments which show hardening are performed at room temperature as well as 120°C and 200°C. Noticeable, experiment u439 (red illite) and u445 (illite without hematite), which started with a normal load of 50 MPa, decreased to 20 MPa and increased again to 50 MPa do show the same evolution of friction trend with displacement. Both experiments are slightly weakening while decreasing in normal load and slightly strengthening while increasing in normal load.

In Figure 9b, the friction coefficients are compared for all the experiments performed on the red illite samples, at room temperature and temperatures of 120°C and 200°C. From the figure it can be concluded that the red illite typically has an apparent friction coefficient ranging from μ_a = ~0.22 – 0.30. The experiments performed at temperatures of 120°C and 200°C show a hardening trend while loading up (expect for the repeat experiment u447), whereas both experiments at room temperature do not show this hardening trend.

Table 7 and Figure 10 shows the linear relation between the shear stress and the effective normal stress for the normal load stepping experiments and the relevant experiment conditions. The straight line fits the data points plotted for the shear stress at each effective normal stress with the relationship $\tau = \mu\sigma_n^{eff} + S_0$. In the table, values are again obtained for the internal friction coefficient (μ) as the gradient and the cohesion (S_0) as the constant for each experiment. The experiments are listed by their type of experiment, e.g. normal load up from 20 MPa or normal load down from 50 MPa, the slopes are listed for both normal load up and down. In Figure 10, the results show the slopes for (a) the normal load up and (b) the normal load down for 20 – 50 – 20 MPa, and Figure 10 (c) show the slopes for normal load up and (d) normal load down for the experiments performed with a starting normal load of 50 MPa – 20 – 50 MPa. Noticeable in the figure is that all the slopes for the normal load up are nearly identical and parallel, whereas for the load down the slopes are much more diverting and not parallel at all, regardless whether the experiment started with a normal load of 20 MPa or 50 MPa.

The linear relations of the slopes show nearly the same values, with an internal friction coefficient for the load up ranging between μ_{int} = ~0.259 – 0.30 and a friction coefficient for the load down with a much wider range of μ_{int} = ~0.21 – 0.33. The results do not show a clear distinction in friction coefficient comparing the sample materials used for the experiments performed at the same conditions. The experiments performed at room temperature and normal load starting at 20 MPa have a coefficient of friction for the red illite of ~0.281, the white illite of ~0.281 and the illite without hematite, slightly lower, of ~0.268. On the other hand, the experiments with normal load starting at 50 MPa showed the opposite, with μ_{int} = 0.261 for the red illite and μ_{int} = 0.292 for the illite without hematite (for the load up).

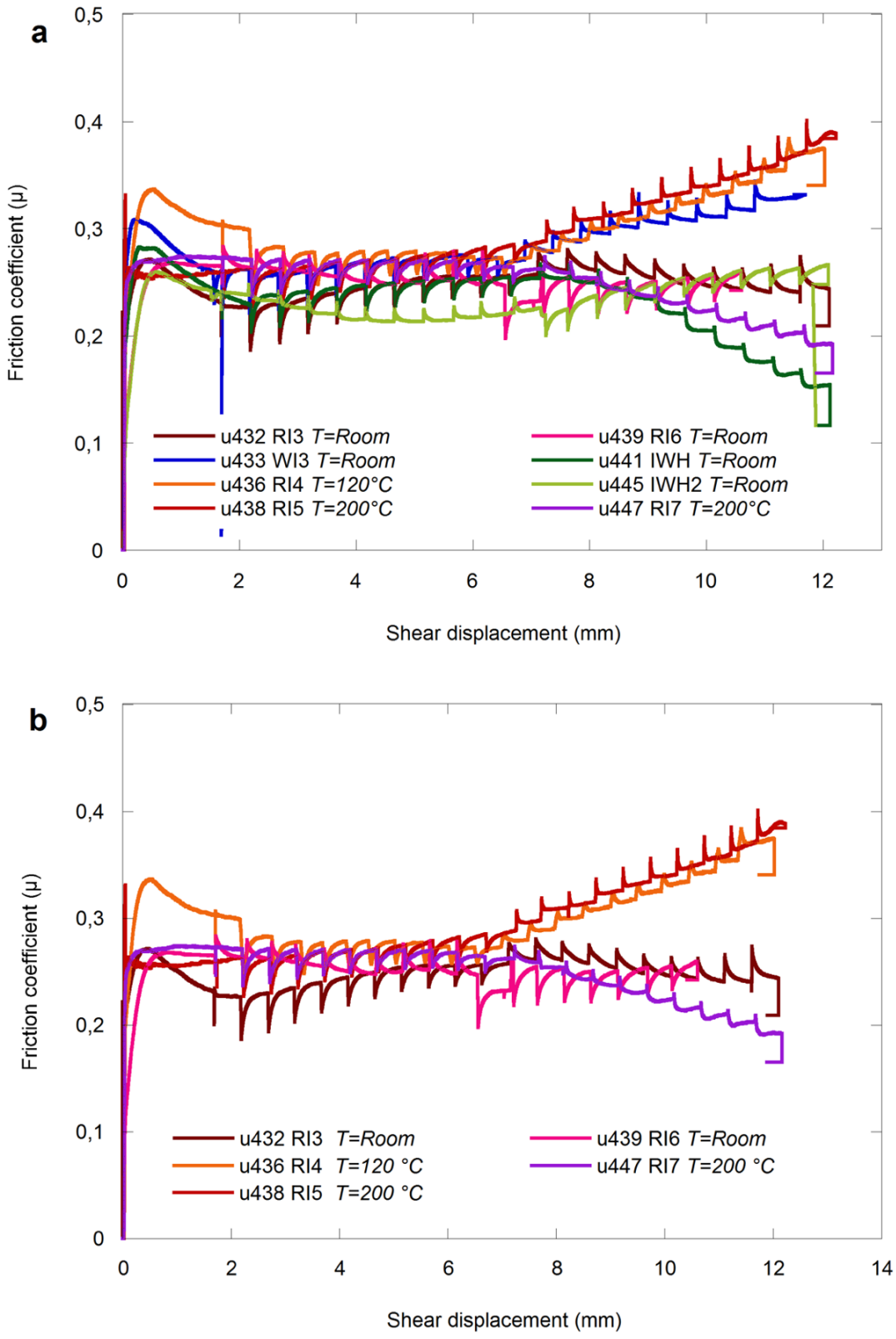

Figure 9: Evolution of the friction coefficient with shear displacement for (a) all normal load experiments u432 – u447 and for (b) all experiment on red illites at room temperature, 120°C and 200°C, normal loads of 20 – 50 MPa (normal load stepping of 3MPa), respectively and fluid pressure of 15MPa.

At the same time, the value of S_0 does not show a systematic trend for the experiments either. Again, the values for S_0 vary the most for the loading down in the experiments compared with the loading up experiments, ranging from S_0 = 3.4 to -4.1. The negative values are unrealistic low values for cohesion. In general, it seems that the experiments performed on the red illite at temperature of 120°C and 200°C have the highest cohesion values with exception of the repeat experiment u447. The cohesion values for the normal load up linear relations are varying between +0.003 and -1.6, which is still too low but much more realistic. Similar for the load up, the experiments performed with the red illite at higher temperature also seem to have the higher cohesion values.

For all experiments the correlation coefficient is approximately ~0.99 which shows a good fit with the data points.

Experiment	**Sample name**	**T (°C)**	**σ_n (MPa)**	**Load up**	**R^2**	**Load down**	**R^2**
u432	Red Illite	Room	20 - 50	y = 0.281x – 0.6616	0.9996	y = 0.2738x – 1.2291	0.9981
u433	White Illite	Room	20 - 50	y = 0.2812x – 1.2935	0.9982	y = 0.2397x + 1.0441	0.9912
u436	Red Illite	120	20 - 50	y = 0.2614x + 0.0028	0.9985	y = 0.2153x + 2.6962	0.989
u438	Red Illite	200	20 - 50	y = 0.3029x – 1.4743	0.9987	y = 0.2176x + 3.4396	0.9817
u441	Illite w/o hematite	Room	20 - 50	y = 0.2686x – 1.1774	0.9999	y = 0.3296x – 4.1589	0.9964
u447	Red Illite	200	20 - 50	y = 0.2594x – 0.2148	0.9991	y = 0.3062x – 2.9042	0.9967
Experiment	**Sample name**	**T (°C)**	**σ_n (MPa)**	**Load down**	**R^2**	**Load up**	**R^2**
u439	Red Illite	Room	50 - 20	y = 0.2764x – 1.2021	0.9983	y = 0.2675x – 1.0054	0.9964
u445	Illite w/o hematite	Room	50 - 20	y = 0.243x – 1.1528	0.9884	y = 0.2923x – 1.9057	0.9996

Table 7: List of the linear relations between shear stress and effective normal stress for experiment normal load stepping experiments, with plot values for the cohesion S_0 as the constant and the friction μ as the gradient in the relationship $\tau = \mu\sigma_n^{eff} + S_0$ (σ_n = applied normal stress in MPa; T = temperature in °C; R^2= correlation coefficient).

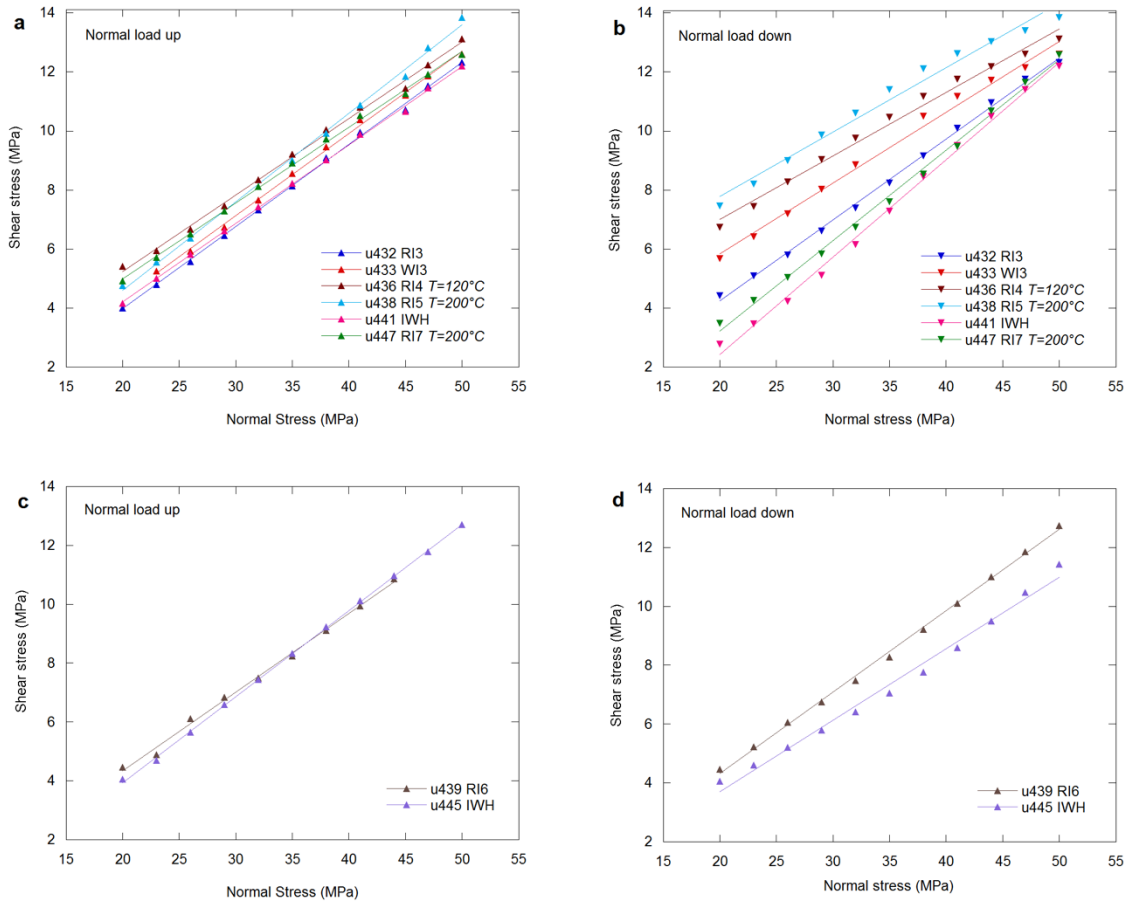

Figure 10: Shear stress vs. effective normal stress for the normal load stepping experiments (a) normal load up stepping experiments u432 – u447 (b) normal load down stepping u432 – u447 for normal load steps of 20 – 50 – 20 MPa at room temperature, 120°C and 200°C and fluid pressure of 15 MPa, (c) normal load up stepping experiments u439 and u445 and (d) normal load down stepping experiments u439 and u445 for normal load steps of 50 – 20 – 50 MPa at room temperature and fluid pressure of 15 MPa. Shear stress values are at steady state. Lines are straight line fit $\boldsymbol{\tau = S_0 + \mu\sigma_n^{eff}}$. Friction coefficients are listed in **Table** 7.

4.1.3 Carmel experiments – normal load and velocity stepping experiments

The evolution of the friction coefficient (μ) versus displacement for the experiments performed on the Carmel CCV-70A sample (u448) and the Carmel sample without hematite (u450) are shown in Figure 11. The experiments, which are performed at room temperature and fluid pressures of 15 MPa both are carried out with normal load stepping as well as velocity stepping. The experiment and sample conditions are listed in Table 5. The total shear displacement for the experiments was ~33.2 mm.

Both experiments show a rapid increase in friction after the start of the experiment with an initial displacement of ~2 mm at an effective normal stress of 20 MPa, after which the velocity stepping and normal load stepping was carried out. For each normal load step (steps of 5 MPa)

velocity stepping is performed at velocities of 1, 10 and 100 μm/s. Figure 11 shows the friction coefficient for both the Carmel CCV-70A sample as well as the Carmel sample without hematite. The apparent μ ranges between μ_a = ~0.5 and ~0.65 which is much higher than the friction coefficients of the experiments performed on the illite samples. This is probably caused by the higher quartz content of ~20% in the Carmel samples.

Overall, the Carmel sample without hematite seems to have a higher friction coefficient than the Carmel CCV-70A sample, especially during the load up stepping of the experiment. While μ of the Carmel CCV-70A sample increases with increasing normal stress, μ of the Carmel sample without hematite decreases with increasing normal stress. At normal stresses of 50 MPa, μ_a = 0.57 – 0.58 for both samples. During the normal load down stepping of the experiment, both samples show overall weakening behavior and μ is approximately the same. For the individual velocity steps, a weakening trend can be observed for the Carmel without hematite samples, in particular during the normal load down, while a strengthening trend can be observed for the Carmel CCV-70A samples.

In Table 8 and Figure 12 the linear relation between the shear stress and the effective normal stress for the normal load stepping experiments is shown. Again, the straight line fits the data points plotted for the shear stress at each effective normal stress with the relationship $\tau = \mu\sigma_n^{eff} + S_0$. In the table, values are again obtained for the friction coefficient (μ) as the gradient and the cohesion (S_0) as the constant for each experiment. From the table, μ is obtained to be μ_{int} = 0.61 for the Carmel CCV-70A sample and μ_{int} = 0.557 for the Carmel sample without hematite during the load up stepping of the experiment, while during the load down stepping of the experiment it is opposite, since μ_{int} = 0.581 for the Carmel CCV-70A sample and μ_{int} = 0.62 for the Carmel sample without hematite. In Figure 12 is showed that the straight line for the Carmel without hematite (u450) is plotted above the Carmel straight line, with higher values of shear stress. Similar for these experiments, the S_0 values are mostly negative, except for the linear relation of the normal load up stepping of the u450 experiment, this can also be observed in the figure. For all experiments the correlation coefficient is approximately ~0.99 which shows a good fit with the data points.

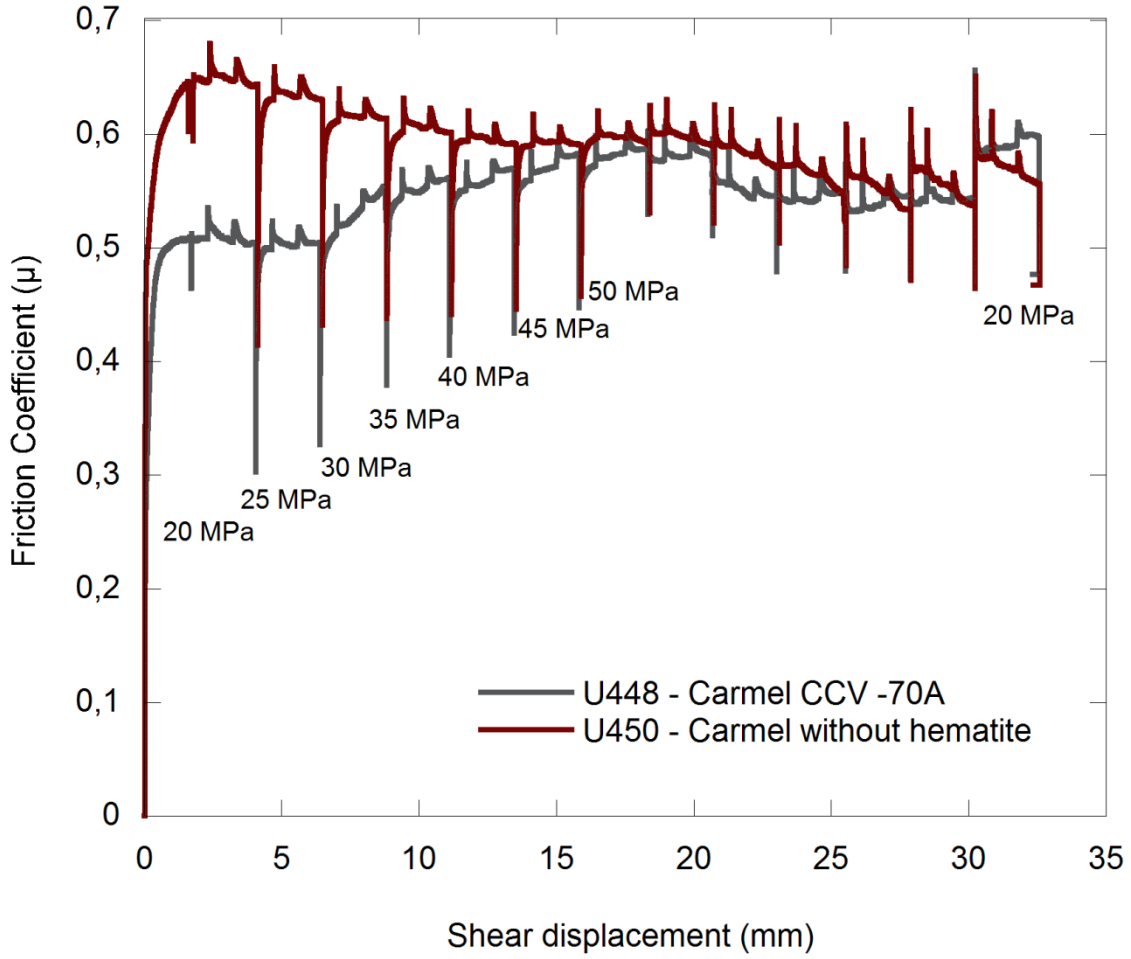

Figure 11: Evolution of the friction coefficient with shear displacement for the Carmel CCV-70A sample and the Carmel sample without hematite at room temperature and normal load of 20 – 50 – 20 MPa with steps of 5 MPa. Velocity stepping is performed for each normal load step with sliding velocities of 1 – 10 – 100 μm/s.

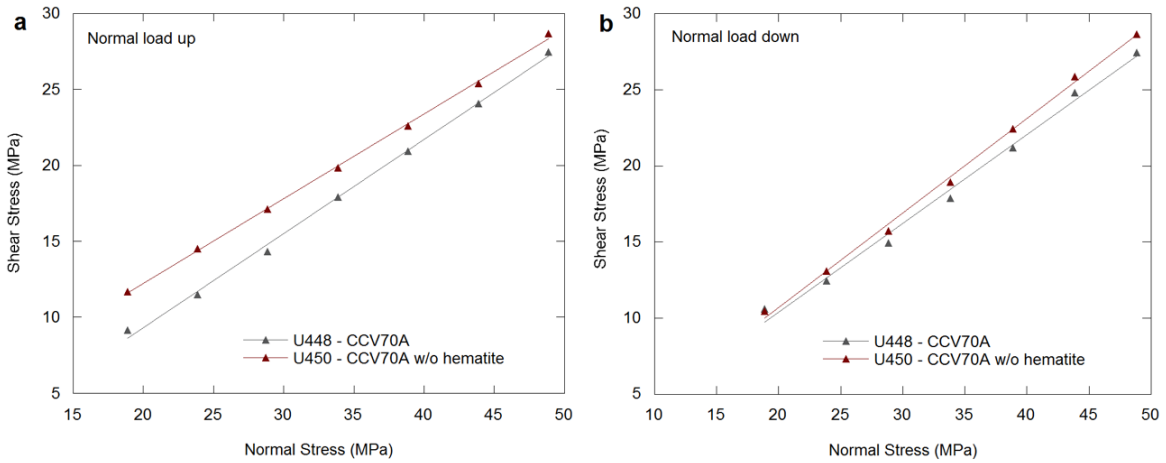

Figure 12: Shear stress vs. effective normal stress for the velocity- and normal stepping experiments of the Carmel samples (u448 and u450). Shear stress values are plotted at steady state. Lines are straight line fit $\boldsymbol{\tau = S_0 + \mu\sigma_n^{eff}}$. Friction coefficients are listed in Table 8. (a) straight line fits during normal load up and (b) straight line fits during normal load down.

Experiment	Sample name	T (°C)	σ_n (MPa)	Load up	R^2	Load down	R^2
u448	Carmel CCV-70A	Room	20 – 50 – 20	y = 0.6184x - 3.7378	0.9975	y = 0.5817x - 1.8769	0.9921
u450	Carmel w/o hematite	Room	20 – 50 – 20	y = 0.5576x + 0.4594	0.9991	y = 0.6199x - 2.391	0.9974

Table 8: List of the linear relations between shear stress and effective normal stress for the Carmel experiments, with plot values for the cohesion $\boldsymbol{S_0}$ as the constant and the friction $\boldsymbol{\mu}$ as the gradient in the relationship $\boldsymbol{\tau = \mu\sigma_n^{eff} + S_0}$ (σ_n = applied normal stress in MPa; T = temperature in °C; R^2= correlation coefficient).

4.1.4 Velocity dependence of friction

The velocity dependence of friction, or *(a-b),* is determined by inverting the Dieterich-type RSF equation (eq. 2) coupled to eq. 4. Examples of the modeled constitutive parameters for the velocity steps are shown in Figure 13, showing positive values for *(a-b)* i.e. velocity strengthening behavior (Figure 13, b and c) as well as negative values, i.e. velocity weakening behavior (Figure 13, a). The modeled constitutive parameters are listed in appendix 1 and 2. Examples are modeled for (a) experiment u450 at velocity step of 10 – 100 µm/s, σ_n^{eff} = 20 MPa, (b) experiment u448 at velocity step of 10 – 100 µm/s, σ_n^{eff} = 40 MPa and (c) experiment u418 at velocity step of 1 – 3 µm/s, σ_n^{eff} = 20 MPa.

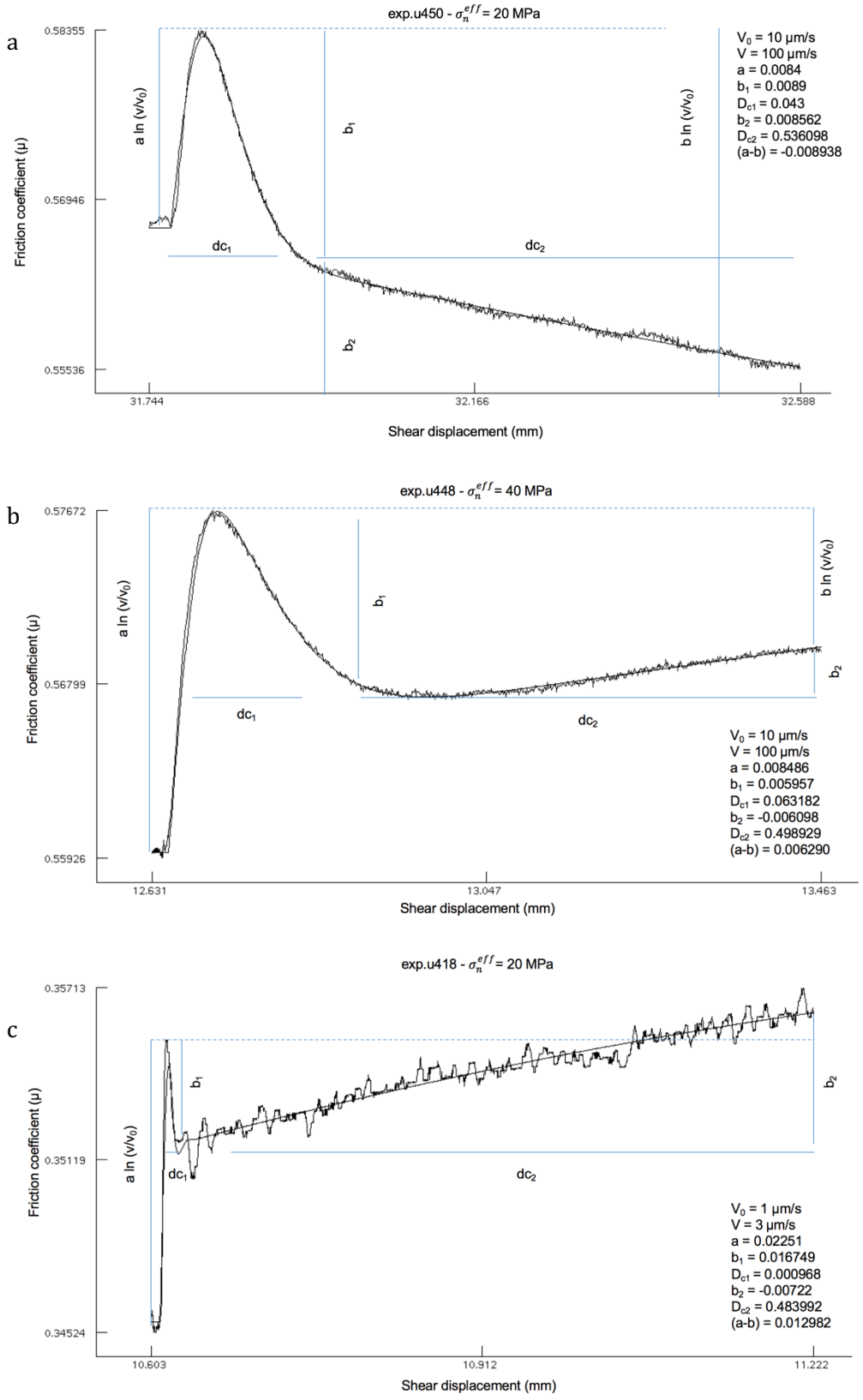

Figure 13: Results for modeling the constitutive parameters a, b (b_1 and b_2), Dc (D_{c1} and D_{c2}) and (a-b) for: (a) experiment u450 – Carmel without hematite experiment at 20 MPa, (b) experiment u448 – Carmel experiment at 40 MPa and (c) experiment u418 – red illite at 20 MPa.

Illite samples - The *(a-b)* values, for the first set of experiments (u416 – u428) on the illite samples, are plotted in Figure 14 as a function of normal load applied and sliding velocity for each separate experiment, performed at constant temperature (room), constant fluid pressure of 15 MPa and normal loads of 20, 27.5 and 35 MPa. Since the velocity steps are repeated, data is illustrated as average *(a-b)* value for each repeated velocity step with the corresponding standard deviations taken as error bar. The standard deviation for all experiments is quite large, showing a large error bar in the graphs. Results indicate that *(a-b)* values are mostly positive for all experiments, indicating mostly velocity strengthening behavior with values ranging between ~0.02 and -0.005. The *(a-b)* values are slightly decreasing with respect to normal stress for the experiments performed on the white illite (u416), red illite (u418) and green illite (u422), even with values slightly below zero at 27.5 MPa and 35 MPa, indicating velocity weakening/neutral behavior at least at higher normal stresses investigated. In experiment u418, u422, u427 and u428, the lowest sliding velocity (i.e. 1 – 3 μm/s) typically shows the lowest *(a-b)* value ranging between 0 and ~0.004, while the highest sliding velocity (i.e. 30 - 100 μm/s) shows higher *(a-b)* values ranging between ~0.004 and ~0.008. Overall, the illite samples do show velocity strengthening behavior (with large error bars ranging in the negative values for some cases) and there does not appear to be a clear relationship between the values of *(a-b)* and mineralogy. Overall, *(a-b)* seems to increase with increasing velocity and decrease with increasing normal stresses.

Carmel samples - The *(a-b)* values, for the experiments (u448 and u450) on the Carmel samples, are plotted in Figure 15 in terms of normal load applied and sliding velocity for each separate experiment, performed at constant temperature (room), constant fluid pressure of 15 MPa and normal loads of 20, 25, 30, 35, 40 and 50 MPa. Since the Carmel experiments are performed with both velocity stepping as well as normal load stepping, the *(a-b)* values are illustrated by the sliding velocity and divided by velocity steps as "normal load up" and "normal load down". In Figure 15, (a) shows the *(a-b)* values for both experiments, during the normal load up, and sliding velocity step of 1 – 10 μm/s. In the figure it can be observed that most values are positive i.e. velocity strengthening with values ranging between 0 and ~0.005. Figure 15b shows the *(a-b)* values also during the normal load up but at sliding velocity step of 10 – 100 μm/s, in this figure the Carmel CCV-70A sample do show mostly positive values, except for the velocity step at 20 and 30 MPa which have slightly negative values close to zero, while the Carmel sample without hematite shows only negative values for all normal loads, with values ranging between 0 and -0.007, i.e. velocity weakening. In Figure 15c *(a-b)* values are plotted for the sliding velocity step of 1 – 10 μm/s during the normal load down of the experiment. Similar to the previous plot, the values for the Carmel without hematite sample shows mainly negative values ranging between -

0.009 and -0.002 for *(a-b)*, i.e. velocity weakening (with 50 MPa as an exception), whereas the Carmel CCV-70A sample is mainly velocity strengthening or neutral with values ranging between ~0.003 and -0.0008. With increasing sliding velocities of 10 – 100 μm/s, the same trend can be observed in Figure 15d. Values of *(a-b)* are decreased even more for both the Carmel CCV-70A samples (~0.003, -0.002) as well as the Carmel samples without hematite (-0.004, -0.012).

In general, the results show that all *(a-b)* values are in a range between ~0.005 and -0.015. *(a-b)* values are typically decreasing with increasing sliding velocity both during normal load up and down. During the normal load down, *(a-b)* values are lower than during normal load up for both samples, showing velocity weakening behavior. Also, *(a-b)* values are in general higher for the Carmel CCV-70A samples than the Carmel samples without hematite, indicating the Carmel samples without hematite to be more velocity-weakening than the Carmel CCV-70A samples.

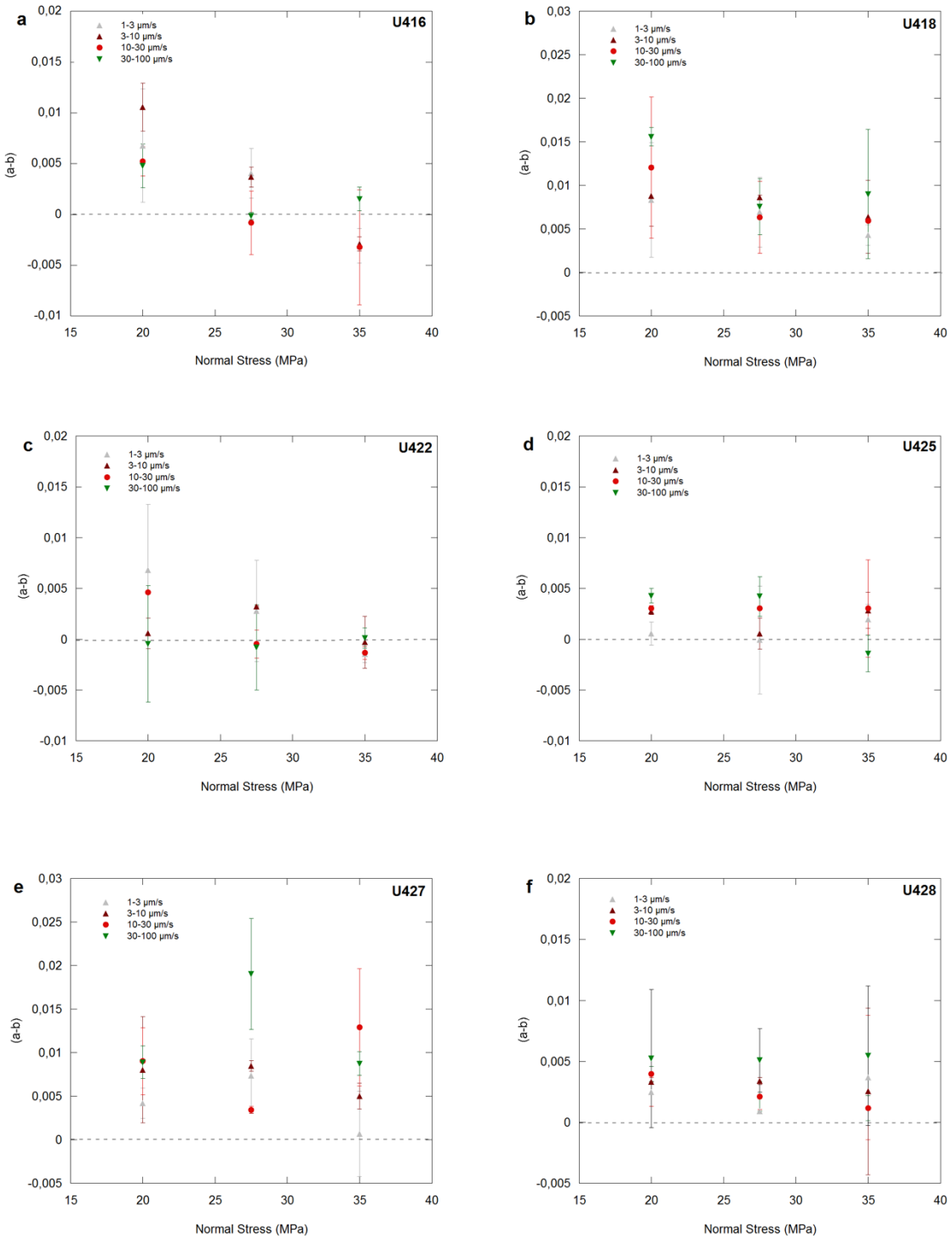

Figure 14: Values of the velocity dependence parameter *(a-b)* versus effective normal stress. The different colors indicate the magnitude of velocity imposed on performing each velocity step. The standard deviation between the repeated velocity steps is indicated as an error bar for each data point. (a) experiment u416 – white illite, (b) experiment u418 – red illite, (c) experiment u422 – green illite, (d) experiment u425 – white illite with extra quartz, (e) experiment u427 – red illite 2 and (f) experiment u428 – white illite 2.

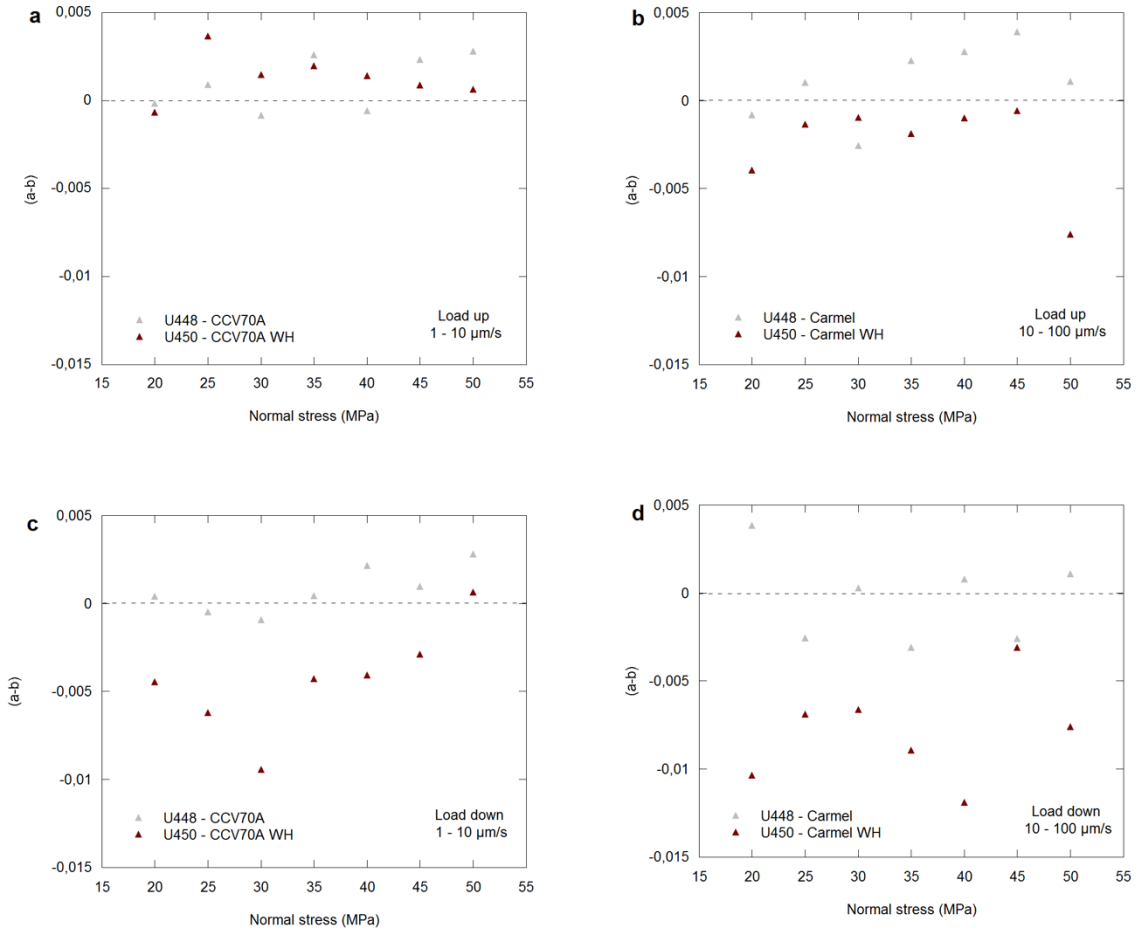

Figure 15: Values of the velocity dependence parameter *(a-b)* for the Carmel samples (u448 and u45) in terms of normal stress applied and sliding velocity for each step for (a) during the normal load up and sliding velocities of 1 – 10 µm/s, (b) normal load up and sliding velocities of 10 – 100 µm/s, (c) normal load down and sliding velocities of 1- 10 µm/s and (d) normal load down and sliding velocities of 10 – 100 µm/s.

5. Discussion

In this report, the long term influence of CO_2 storage on the frictional strength of clay-rich rocks is investigated by performing friction experiments using a ring shear apparatus on clay samples with varying mineral compositions and contents of hematite. For CO_2 storage to be a viable option for mitigating climate change, it is important to understand the risks associated, such as the potential leakage of CO_2 along (reactivated) faults and potential induced seismicity due to the reactivation of faults. Here, the potential effects of long term interaction between CO_2, brine and rock on the mechanical and transport properties on clay rich rocks (caprock) is investigated, since preliminary experiments on samples from the Carmel Formation (illite-rich clays) showed that small differences in mineralogy (in particular the presence or absence of hematite) could have significantly influence on the friction strength of rocks.

Ring shear experiments are performed using clay samples with varying mineralogy and contents of hematite by performing velocity stepping experiments as well as normal load stepping experiments. The effect of the mineralogy on the frictional properties is investigated, as well as the effect of hematite and the type of experiment on the frictional properties. Here, results will be compared and findings will be explained compared with literature.

5.1 Mineralogy quantification of the samples by XRD and ICP

The intention in this study was to use mostly illite-rich clay samples. However, XRD analysis showed that the clay samples turned out to be not pure illites, but a mixture of different clay minerals, like kaolinite, dickite, phengite, microcline and quartz as described in section 3.2. In here, the uncertainties in the XRD and ICP analysis will be described. First of all, as described earlier, quantification of clay minerals is difficult in general, since the individual peaks of the minerals are hard to distinguish (see section 3.2.2). Also, since most clay minerals (i.e. illite and microcline) contain K, Al and Si, the quantification of the clay minerals depends on the ratios of these elements in the sample. The ratio between the clay minerals is therefore in some cases difficult to identify, which can result in some uncertainties regarding the quantification of the sample mineralogy. Depending on the ratio of the clay minerals, the quartz content generally has a small uncertainty of ± 0.1 – 1% (Table 3). The ICP calculations of the clay samples indicated that in most samples only about 15 – 38% illite was present. However, the uncertainties in the ICP analysis must also be included, for example, the quantification of the sample mineralogy is only based on the ICP analysis which is only performed once for each sample. Besides, the outcome of the ICP analysis has some small uncertainties as well, since the values below the detection limit are not measured, and values below the Background Equivalent Concentration can have a small error of > 10% (Table 2). However, this does not involve the main elements present in the clay

minerals and the uncertainties are therefore very small. Overall, the main differences in composition between the samples, as listed in Table 3, are within the illite content which ranges between 15% - 38%, with the white illite and green illite having the lowest illite content and the red illite the highest illite content. The quartz content ranges between 1.5% - 20%, with the Carmel CCV-70A sample having the highest quartz content (~20%) and the white illite having the lowest quartz content (~1.5%). Furthermore, kaolinite (17% – 40% in red illite and green illite) and dickite (~75% in white illite) and phyllosilicate mica minerals like phengite (11% - 38%) are present. Hematite is only present in the red illite sample and the Carmel CCV-70A sample with contents of 2.9% and 1.3%, respectively.

5.2 Effect of mineralogy on the frictional properties

Since the clay samples used in this study are not pure illites, but mixtures of other (clay) minerals (kaolinite, microcline, dickite and phengite) and small contributions of quartz, a comparison has to made between the different samples to be able to find a relation between the mineralogy and the frictional properties. Velocity stepping and normal load stepping experiments performed on the clay samples showed slightly differing results for the friction strength, although overall, all the clay samples are ranging between μ = 0.20 and μ = 0.38 (Table 6 and Table 7) which are typical values for sheet silicates as reported by Moore & Lockner, 2004 and Tembe, Lockner, & Wong, 2010, as μ = 0.2 – 0.5. All samples contain approximately 15 – 38% illite. The main difference in mineralogy are within the amount of dickite (~75%) in the white illite, phengite (~40%) in the green illite, kaolinite (~40%) in the red illite and the variations in quartz content (Table 3).

Generally, pure quartz has a friction coefficient of ~0.49 – 0.62 (Logan & Rauenzahn, 1987), therefore samples containing more quartz generally have higher μ compared with clays. The velocity stepping series of experiments show white illite (containing 75% dickite, 15% illite, 7% microcline and 1,5% quartz) to be the weakest with μ = ~0.20, followed by the red illite and green illite μ = ~0.30 – 0.35. The low friction of the white illite is in agreement with Tembe, Lockner, & Wong, 2010, who report that the coefficient of friction generally decreases with increasing clay content and white illite has the highest clay content and lowest quartz content. Furthermore, illite is within the 2:1 sheet silicate group, which is reported to be weaker than the 1:1 sheet silicate group (kaolinite and dickite) (Morrow, Moore, & Lockner, 2000; Moore & Lockner, 2004).

The higher friction coefficient of the red and green illite could be explained by the higher amount of quartz in the green illite (~12%) and red illite (~7%), the presence of hematite in the red illite (~3%) or the phengite in the samples. (RI: ~13% and GI: ~38%). Since phengite is a di-octahedral mica and a variety of muscovite with addition of magnesium (Mg) (Güven, 1967) and micas

generally also have a low friction coefficient, the higher friction is possibly caused by the presence of hematite and/or higher quartz contents. The effect of quartz on μ is clearly visible in the experiment with the white illite and the extra quartz added (total quartz of ~40%), since the rest of the mineralogy is the same. The white illite sample with extra quartz shows μ = 0.46, which is more in the range of pure quartz friction. Although the variations in friction are small, it seems like the relative amounts of quartz and clay have a significant influence on the friction coefficient, rather than the type of clay since they are mostly clay mixtures.

All clay samples in this study shows velocity strengthening behavior with minor variations in *(a-b)* values with increasing velocity and normal load, which is corresponding with previous studies, reporting positive *(a-b)* values and velocity strengthening behavior for clay mixtures (Saffer & Marone, 2003; Tembe, Lockner, & Wong, 2010). This would indicate that the mineralogy of clays in this study has no (large) influence on the velocity dependence of friction.

The results of the normal load stepping experiments do show the same results as the velocity stepping series of experiments regarding the coefficient of friction. All the experiments performed on the red illite, white illite and red illite without hematite show μ in a range of ~0.22 – 0.30 during the normal load up stepping of the experiment. These series of experiment do not show a clear relation between the mineralogy of the samples and the frictional properties either as they all show a typical coefficient of friction for clays.

5.3 Effect of hematite on the frictional properties

Besides considering the clay mineralogy, the coefficient of friction could also be influenced by the presence of hematite. Studies have shown that clay minerals tend to flocculate more easily with the presence of hematite, and flocculated samples have higher resistance and higher shear strength (Ohtsubo & Yoshimura, 1991; Pillai, et al., 2010).

The velocity stepping and normal load stepping experiments are performed on red illite samples containing ~3% hematite and Carmel samples containing ~1,5% hematite as well as samples containing no (0%) hematite (i.e. white illite, green illite and red illite without hematite). Results show that the overall friction coefficient (μ) of the red illite with hematite is generally between ~0.261 and ~0.313 for all experiments performed. The Carmel CCV-70A sample is far richer in quartz (~20%) than the red illite (~7.8%) and the effect is clearly visible in the friction coefficient which is in the range between ~0.58 and ~0.61.

The effect of hematite on the frictional properties can be best compared with the same sample materials used for the sodium dithionite procedure at which the hematite is removed from the samples and mineral composition is similar (see mineral composition in Table 3 for red illite (RI)

and red illite without hematite (RIWH)). These results showed μ to be between the range of ~0.243 and ~0.329. At first glance, no significant difference of μ is present compared with the results of the illite without hematite samples, but when comparing the values separately for the normal load up and normal load down, μ is slightly lower during the normal load up (RI: μ = 0.281 and RIWH, μ = 0.268) and slightly higher during the normal load down (RI: μ = 0.274 and RIWH, μ = 0.323) at room temperature. On the other hand, the experiments performed with a starting normal load of 50 MPa, show the opposite trend. However, it is clear that the overall friction for the illite, with and without hematite, varies between μ = 0.26 and 0.32 approximately, which is a value comparable with other studies, which show values for illite and kaolinite to be in the order of μ = ~0.29 – 0.40 (Behnsen & Faulkner, 2012). Note that the Carmel sample contains more quartz, resulting in a friction coefficient higher than the illite sample (μ = 0.58 (normal load down) – 0.61 (normal load up)). From XRD and ICP analysis it can be concluded that the Carmel samples are not pure clays, since it contains more quartz and also dolomite, calcite and albite (Table 3). In this case, there is again no clear difference between the friction coefficient of the samples containing hematite or not, since the sample processed with the sodium dithionite procedure show μ to be ~0.56 (normal load up) and ~0.62 (normal load down). Similar as with the illite clays, μ of Carmel without hematite is slightly lower during load up, while μ is slightly higher during load down. In both cases, there does not seem to be a clear effect of hematite on the frictional strength (or μ) of the clay-rich rocks.

However, the velocity dependence of friction, *(a-b)*, does show an effect of hematite on *(a-b)* since the Carmel without hematite samples show systematically lower values of *(a-b)* and they have generally all velocity weakening behavior, indicating potentially unstable slip while the Carmel samples do show velocity strengthening behavior. This would indicate that the absence of hematite can generate velocity weakening behavior. Note that the largest difference between the *(a-b)* values is observed during the load down of the experiment (Figure 15b and d).

5.4 Effect of type of experiment

As discussed in section 5.2 and 5.3, the largest variations between the frictional properties of the different sample materials used in this study are observed during the normal load stepping experiments, in which the normal load is either increased (normal load up) or decreased (normal load down). It is apparent in Figure 10 that the variation in friction is much larger during the normal load down stepping than during the normal load up stepping, similar for the velocity dependence of friction, results show the largest variations in *(a-b)* values during the load down than the load up of the experiments (Figure 15). There clearly is an effect of the type of experiment

(i.e. normal load up vs. down) since the results during the normal load up seem to be more consistent than during the normal load down.

There are several reasons that can explain variations in friction during the experiments. The first uncertainty is within the sample material; for each experiment new sample material is used and sample material is not reused. Assuming the sample material is not completely homogeneous, this could possibly lead to small differences in mineralogy or grain size within the sample material. Furthermore, fluctuations in the process of sample preparations and ring pressing could also cause variations in friction due to variations in layer thickness, porosity and sample and water weight. During the experiment itself, settings of the experiment could also cause variations in friction, like fluctuations in temperature, pore fluid or fluctuations in the start set up of the experiments and the type of piston set used. Since the experiments in this study are mostly carried out on room temperature it is not likely that large variations in temperature have occurred. Also, all experiments are performed using the same piston set (HT-2) except for experiment u428 (piston set HT-1).

In addition, the ring shear device itself has uncertainties that could influence the friction results. For example, the seal friction can fluctuate and can cause uncertainties from experiment to experiment. The externally measured shear stress, should be corrected for the friction exerted by the dynamic seals. From previous calibrations the seal friction is calculated to be ~1.9136 MPa normal stress. In these experiments, seal correction is calculated from the data to be ~0.784 MPa ± 0.238 MPa. Except for seal friction in normal load, the seals also do have shear stress friction, which is the friction that is caused by rotating. In Figure 16 the shear stress friction of the seal is shown (exp. u427), for ~48.4 mm of rotation (note that one whole rotation is ~78 mm). One rotation shows a maximum variation in friction of ± 1,6 MPa, depending on the starting position of the vessel. A few mm in difference of starting position can therefore lead to a small deviation in shear stress. Taking into account the fact that the experiments performed in this study are mostly carried out at relatively low normal loads (e.g. 20 MPa) and the friction coefficient is a function of the shear stress and normal stress, $\mu = \tau/\sigma_n$, the variation in seal friction have less of an effect on friction with increasing normal load and variations are largest at low normal loads.

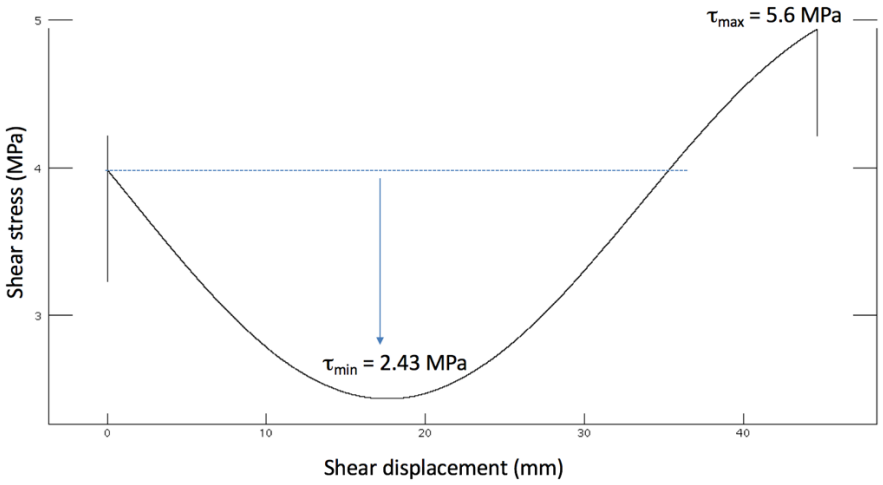

Figure 16: Shear displacement (mm) versus shear stress of the seals (MPa) for ~48.4 mm of one rotation (note that one whole rotation is 78 mm), showing the minimum shear stress (~2.43 MPa) and the maximum shear stress (~5.6 MPa). The average shear stress of the seals is ~4 MPa, indicating an uncertainty of ± ~1.6 MPa.

Figure 17 shows the shear stress versus normal stress for the normal load stepping experiments when corrected for the (maximum) seal friction as a large uncertainty area indicated by the grey lines. The uncertainty of the linear relation is quite large, considering the maximum seal correction for the shear stress of ± 1.6 MPa and the seal correction for the normal stress of ~0.784 MPa. The negative cohesion values of most sample materials are, when corrected for seal friction, not negative anymore and could therefore be explained by the corrections in seal friction. However, even when corrected for seal friction, some cohesion values are still negative. The low cohesion values are clearly not only related to the seal correction. Therefore, another explanation for the extremely low cohesion values in, for example, repeat experiment u427 with S_0 = -8.02 is discussed.

The low cohesion values could be related to the layer thickness of the sample. All velocity stepping experiment have a final sample thickness of ~0.95 – 1.18 mm, except for the repeat experiment which has a final thickness of 0.30 mm. Layer thinning of a sample layer occurs during an experiment due to initial compaction of the layer by the application of normal load or the escape of sample material through small gaps between the rings and the piston, causing loss of sample material. Considering the low final layer thickness of the u427 sample compared to the other samples, the extremely negative cohesion is probably related to this thin layer thickness. A possible explanation is that the normal stress is not supported by the layer but by the pin in the center of the sample assembly and the result of normal stress vs. shear stress are therefore not really reliable.

Except for uncertainties in seal friction, the large variations in the friction coefficient during the load down experiments could also be related to the layer thickness and compaction of the sample material. The large variations in the friction coefficient during the load down, are visible for the experiments starting with a load up (start at 20 MPa) as well as for experiments starting with a load down (start at 50 MPa). The variations in normal load down seem to be none dependent whether the experiment started with the load down or load up. During the load up of an experiment, the sample layer will receive more load and compaction of the layer will take place, while during the normal load down of the experiment the normal load on the sample will get less, and the sample layer will possibly de-compact a little, which could maybe result in the larger variations of the normal load down, since this de-compaction will not be the same for all sample materials.

Earlier the difference in the velocity dependence of friction was discussed between the Carmel experiment (u448) and the Carmel experiment without hematite (u450), taken into account all the uncertainties the device and experiment itself can have, it is useful to compare these uncertainties. First of all, no difference in final layer thickness has been observed, since both experiments have a final layer thickness of ~0,72 mm and ~0,65 mm layer, for the Carmel and Carmel without hematite, respectively. Since the results showed that the Carmel samples without hematite are showing lower, and negative, values of *(a-b)* indicating velocity weakening behavior for each velocity step, layer thickness (or vertical displacement) for each individual velocity step is also compared. The vertical displacement of each individual velocity step is compared, to see if there is any relationship between the vertical displacement and the velocity dependence of friction. Both the Carmel sample as well as the Carmel sample without hematite showed approximately the same vertical displacement in each velocity step. Furthermore, since both experiments are performed at room temperature, there are no fluctuations in temperature. Also, no fluctuations in fluid pressure are observed during the experiments. The differences in the velocity dependence of friction are therefore not considered to be a result of experimental uncertainties, but are probably caused by (mineralogy) differences in the sample material itself i.e. the presence or absence of hematite.

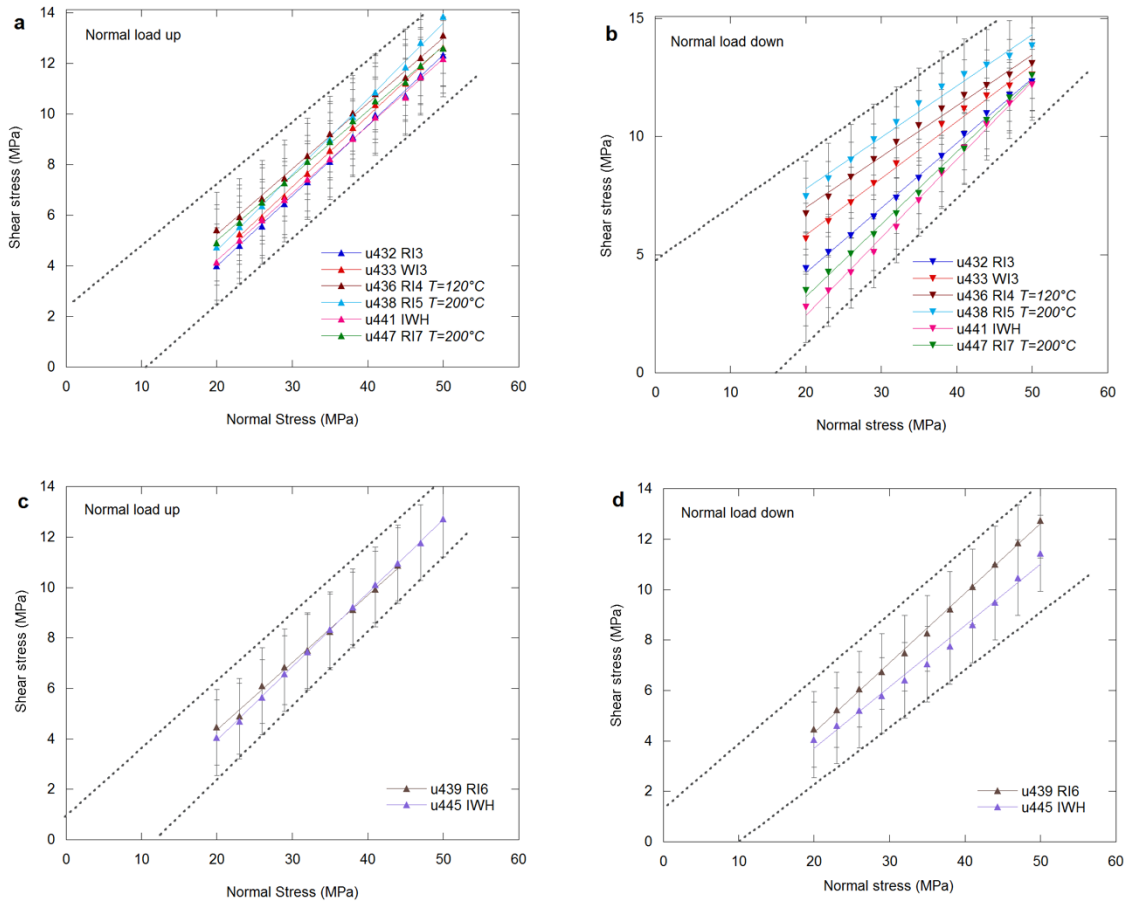

Figure 17: Shear stress vs. effective normal stress for the normal load stepping experiment, showing the maximum uncertainty range based on the correction of the seal friction. Grey lines are indicating the maximum and minimum shear stress uncertainty.

5.5 Implications for CO_2 capture and storage (CCS)

Earlier in this report, the effects of mineralogy and in particular the effects of hematite on the frictional properties of clay-rich rocks are investigated, to assess the long term influence of CO_2 storage on fault friction. To capture CO_2 at the source and store it in depleted oil and gas reservoirs, deep saline aquifers or unmineable coals seems, it is important to understand the geochemical behavior of carbon dioxide storage in geological reservoirs over short and long timescale to ensure storage integrity. The results from the velocity and normal load stepping experiments performed in this study are important for understanding the frictional and fault behavior of clay rich samples with different mineralogy, but the main question was if the small variations in mineralogy, and in particular the presence or absence of hematite has any significant effect on fault strength or frictional stability and the implications for CO_2 capture and storage.

First of all, previous studies suggested that samples taken from a natural CO_2 reservoir near Green River, Utah showed bleached zones within the caprock, related to CO_2 penetration. The bleached zones showed significant differences in mineralogy since all the hematite present in the unbleached zones was completely dissolved and other minerals were precipitated (Kampman, et al., 2013; Busch, et al., 2014). However, our results indicated that the bleaching of the caprock (i.e. dissolution of hematite) does not have any effect on the frictional properties of the clay samples since there are no clear differences in the coefficient of friction between the Carmel samples and the Carmel samples without hematite (μ = ~0.58 – 0.61). Furthermore, from the pure illite experiments, it is apparent in all of the samples examined, with different contents of hematite, illite, kaolinite, dickite, phengite and quartz that the coefficients of friction are around ~0.20 – 0.38, showing no significant difference between the hematite contents and the coefficient of friction. In this study, different clay samples (illite, kaolinite, phengite and dickite) have been tested, as well as different contents of hematite and quartz, to simulate differences in mineralogy. In general, our values of coefficient of friction for clay minerals are in agreement with previous studies about friction of clays. This would indicate that the storage of CO_2 in depleted oil and gas reservoirs, which could potentially lead to bleached zones (i.e. dissolution of hematite) and varieties of mineral reactions, has no (clear) effect on the frictional strength of the clay-rich rocks. However, our results showed that the amount of quartz present in the samples has a large effect on the coefficient of friction, since adding quartz to the white illite clay increases the friction coefficient from μ_a = ~0.20 – 0.35 for the white illite samples to μ_a = ~0.30 – 0.40 for the white illite samples with extra quartz added. As described earlier, several reactions can occur in rocks involving CO_2 besides the dissolution of hematite (section 1). One of the reactions that could possibly occur is the precipitation of clays (e.g. illite, kaolinite). Considering the fact that clays are typically weak and our experiments confirm that extra quartz increases the coefficient of friction,

precipitation of clays would decrease the coefficient of friction. So if for example CO_2 fluid would leak along pre-existing quartz bearing faults, the precipitation of clays could weaken the fault and be possibly be reactivated.

On the other hand, our results as well as previous studies have shown that clay samples (exp. u416 – u428, Figure 14) generally show velocity strengthening behavior (Saffer & Marone, 2003; Tembe, Lockner, & Wong, 2010). However, the results of the velocity dependence of friction in case of the Carmel samples (Figure 15), did show results that could potentially indicate that the CO_2 storage could lead to velocity weakening behavior since all results from the Carmel experiments without hematite showed negative *(a-b)* values (Figure 15), indicating potentially unstable slip. The results showed that the dissolution of hematite, at least in the Carmel samples, result in lower *(a-b)* values, in most cases negative. The lower *(a-b)* values can be caused by either a smaller "*a*" or a larger "*b*", which would give an indication for the mechanism responsible.

In the case of the Carmel samples without hematite, the value of *a* is mostly a bit larger during the load up and smaller during the load down than the values of *a* for the Carmel samples. The *b* value is also a bit larger during the load up and smaller during the load down than the values for the Carmel samples, resulting in lower *(a-b)* values (again, the differences are largest during the load down of the experiments) (for the modeled constitutive parameters, see appendix 1 and 2). Studies have interpreted the value *b* to be a measure of frictional strength change due to evolution of contact surfaces (Ikari, Marone, & Saffer, 2009). According to Saffer & Marone, 2003, at low velocities when the *b* values are approaching zero, the mineral surfaces are in complete contact and the real area of contact does not change after a velocity step (concept of contact saturation). So when particles are horizontally aligned (i.e. dispersed) and mineral surfaces are in complete contact the *b* value tend to be lower and approach zero. In the case of the Carmel samples, studies have shown that clay minerals tend to flocculate more easily with the presence of hematite (Arias, et al., 1995; Pillai, et al., 2010), while usually clay minerals are dispersed arranged. An explanation for the negative *(a-b)* values could be that in case of the Carmel samples with hematite, where the grains could be flocculated, and the Carmel samples without hematite, where the grains are dispersed arranged and horizontally orientated, the contact area of the Carmel samples without hematite is larger and therefore the *b* value should be lower. This would imply that the value of *a* should be smaller too, in the case that the *(a-b)* value is negative. However, in the results it is not completely clear whether the negative *(a-b)* is caused by the value of *a* or *b,* since there are differences between the load up and load down as well, and therefore it is hard to indicate the mechanism responsible.

Overall, if bleaching (i.e. the dissolution of hematite) by CO_2 of clay-rich caprock would lead to unstable slip (negative (*a*-*b*) values), this would mean that on the long term, potentially clay-rich faults capping potential CO_2-reservoirs if reactivated can generate earthquakes (i.e. induced seismicity).

However, since the results are based on only 2 experiments from the Carmel formation and both experiments are performed on room temperature, more research on the Carmel samples has to be done with, for example, experiments at higher temperatures. In addition, experiments on samples from other natural CO_2 reservoirs could be done to investigate if bleaching by CO_2 (the absence of presence of hematite) really changes the velocity-dependence of friction.

6. Conclusion

Velocity stepping and normal load stepping experiments are performed on a hydrothermal ring shear apparatus in the High Pressure and Temperature Laboratory at the Utrecht University, on a series of (illite) clay samples and samples obtained from the Carmel Formation near Green River, Utah. The experiments are performed on samples, with varying illite, kaolinite, quartz and hematite contents at room temperature, using a fluid pressure (P_f) of 15 MPa and σ_n^{eff} of 20 – 50 MPa to simulate in-situ reservoir conditions, in terms of stress and fluid pressure. The aim of this study was to investigate the long-term effect of CO_2 storage on the mineralogy and in particular the hematite on the frictional properties of clay rich rocks.

The following conclusions are made based on the results from the friction experiments:

1. Bulk XRD analysis of clay samples does not give reliable quantitative data. Combined with ICP analysis, samples used in this study contained 15% - 38% illite and 1,5% - 20% quartz, with the Carmel CCV-70A sample having the highest quartz content (~20%) and the white illite having the lowest quartz content (~1.5%). Other phyllosilicate clay minerals (kaolinite and dickite) and phyllosilicate mica minerals (phengite) were present. Hematite was present in the red illite (2.9%) and the Carmel CCV-70A (1.3%). A sodium dithionite procedure is performed successfully on the red illite and Carmel sample to simulate hematite dissolution.
2. The coefficient of friction for the illite samples is found to be ~0.20 – 0.38. The least quartz-rich white illite sample shows the lowest friction, μ = ~0.20, followed by the red illite and green illite μ =~0.30–0.35. Overall, the illite samples show velocity strengthening behavior (at room temperature, P_f = 15 MPa, σ_n^{eff} = 20, 27.5 and 35 MPa). The *(a-b)* values increase with increasing velocity and decrease with increasing normal stress.
3. The most quartz-rich samples (~20%), the Carmel sample and the Carmel without hematite sample, have the highest coefficient of friction of ~0.56–0.61 (at room temperature, P_f = 15 MPa, σ_n^{eff} = 20 - 50 MPa). When extra quartz added to the white illite sample, the coefficient of friction increases from μ_a = ~0.20 – 0.35 to μ_a = ~0.30 – 0.40.
4. Both series of experiment (illite samples and Carmel samples) show no (clear) effect of varying hematite content (0%, 1.5% and 3% hematite) on the frictional strength of the samples.
5. The Carmel samples show higher *(a-b)* values than the Carmel samples without hematite, which show mostly negative values. The Carmel samples without hematite show velocity weakening behavior. Overall, *(a-b)* values are decreasing with increasing sliding velocities (sliding velocities of 1 – 10 and 10 – 100 μm/s).

6. Normal load stepping (load up and load down) as well as velocity stepping experiments are performed. Most variations in the coefficients of friction and velocity dependence of friction have been observed during the normal load down of the experiments compared with the normal load up.
7. The negative values for the velocity dependence parameter *(a-b)* for the Carmel samples without hematite indicate that the absence of hematite in the Carmel caprock could potentially lead to velocity weakening behavior, i.e. unstable slip. This potentially means, that bleaching of clay-rich caprock of faults by CO_2 (dissolution of hematite), could potentially lead unstable slip (i.e. earthquakes) once a fault is reactivated in potential CO_2 reservoirs. However, the presence or absence of hematite does not have a significant influence on the frictional strength of clay-rich rocks, tested in this study.

7. Acknowledgements

First of all, I would like to thank Dr. André Niemeijer and Dr. Suzanne Hangx for assisting me through this master thesis project, discussing the results and assist me in the lab. Furthermore, I would like to thank Sabine Den Hartog and Bart Verberne for assisting me with the ring shear apparatus. Special thanks to Peter van Krieken, who helped me through the chemical procedures in the lab and performed the XRD and ICP analysis. And last, to all master students in the master room for their nice support during the coffee breaks of this master thesis project.

8. References

Arias, M., Barral, M., & Diaz-Fierros, F. (1995). Effects of iron and aluminium oxides on the colloidal and surface properties of kaolin. *Clay and clay minerals*(43), 406-416.

Bachu, S., Gunter, W., & Perkins, E. (1994). Aquifer disposal of CO2: Hydrodynamic and mineral trapping. *Energy Conrers. Mgmt Vol. 35, No. 4*, pp. 269-279.

Baines, S., & Worden, R. (2004). The long-term fate of CO2 in the subsurface: natural analogues for CO2 storage. *Geological Society*(233), 59-85.

Behnsen, J., & Faulkner, D. R. (2012). The effect of mineralogy and effective normal stress on frictional strength of sheet silicates. *Journal of Structural Geology*(42), 49-61.

Blackmore, A. (1973). Aggregation of clay by the products of iron (III) hydrolysis. *Australian Journal of Soil Research*(11), 75-82.

Busch, A., Kampman, N., Hangx, S. J., Snippe, J., Bickle, M., Bertier, P., . . . Schaller, M. (2014). The Green River natural analogue as a field laboratory to study the long term fate of CO2 in the subsurface. *Energy Procedia*, 2821-2830.

Byerlee, J. (1978). Friction of rocks. *Pure Appl. Geophys.*(116), 4-5.

Den Hartog, S., & Spiers, C. (2013). Influence of subduction zone conditions and gouge composition on frictional slip stability of megathrust faults. *Tectonophysics*(600), 75-90.

Den Hartog, S., Peach, C. J., De Winter, D., Spiers, C., & Shimamoto, T. (2012). Frictional properties of megathrust fault gouges at low sliding velocities: New data on effects of normal stress and temperature. *Journal of Structural Geology 38*, 156-171.

Dieterich, J. H. (1978). Time-Dependent Friction and the Mechanics of Stick-Slip. *Pure Appl. Geophys 116*, 790-806.

Dieterich, J. H. (1979). Modeling of rock friction: 2. Simulation of preseismic slip. *Journal of Geophysical Research 84*, 2169-2175.

Dieterich, J. H. (1981). Consitutive properties of faults with simulated gouge. *Mechanical Behavior of Crustal Rocks: The Handin Volume*, 103-120.

Güven, N. (1967). The crystal structure of 2M1 phengite and 2M1 muscovite. *Carnegie Inst. Washington Year Book*(66), 487-492.

Giese, R. (1978). The electrostatic interlayer forces of layer structure minerals. *Clay and clay minerals*, 51-57.

Hangx, S., Bakker, E., Bertier, P., Nover, G., & Busch, A. (2015). Chemical–mechanical coupling observed for depleted oil reservoirs subjected to long-term CO2-exposure – A case study of the Werkendam natural CO2 analogue field. *Earth and planet science letters 428*, 230-242.

Hitchon, B. (1996). Aquifer Disposal of Carbon Dioxide: Hydrodynamic and Mineral Trapping . *Geoscience Publishing Ltd*, 165.

Ikari, M. J., Marone, D. M., & Saffer, C. (2009). Frictional and hydrologic properties of clay-rich fault gouge. *Journal of Geophysical Research*(114), B05409.

Kampman, N., Bickle, M., Maskell, A., Chapman, H., Evans, J., Purser, G., . . . Busch, A. (2014). Drilling and sampling a natural CO2 reservoir: Implications for fluid flow and CO2-fluid-rock reactions during CO2 migration through the overburden. *369*, 51-82.

Kampman, N., Maskell, A., Bickle, J., Schaller, M., Purser, G., Zhou, Z., . . . Busch, A. S. (2013). Scientific drilling and downhole fluid sampling of a natural CO2 reservoir, Green River, Utah. *Scientific Drilling*(16), 33-43.

Logan, J., & Rauenzahn, K. (1987). Frictional dependence of gouge mixtures of quartz and montmorillonite on velocity, composition and fabric. *Tectonophysics*(144), 87-108.

Marone, C. (1998). Laboratory derived friction laws and their application to seismic faulting. *Annu. Rev. Earth Planet. Sci*(26), 43-96.

Metz, B., Davidson, O., de Coninck, H., Loos, M., & Meyer, L. (2005). *Special IPCC Report on Carbon Dioxide Capture and Storage, working group III of the Intergovernmental Panel on Climate Change.* Cambridge and New York: Cambridge University Press.

Michalet, R., Guillet, B., & Souchier, B. (1993). Hematite identification in pseudoparticles of Moroccan rubified soils. *Clay minerals*(28), 233-242.

Moore, D. (1997). X-Ray Diffraction and the Identification and Analysis of Clay minerals. *Oxford University Press, 2*, -.

Moore, D., & Lockner, D. (2004). Crystallographic controls on the frictional behavior of dry and water-staturated sheet structure minerals. *Journal of geophysical research*(109), B03401.

Morrow, C., Moore, D., & Lockner, D. (2000). The effect of mineral bond strength and adsorbed water on fault gouge frictional strength. *Geophysical Research Letters*(27), 815-818.

Morrow, C., Radney, B., & Byerlee, J. (1992). Frictional Strength and the Effective Pressure Law of Montmorillonite and Illite Clays. In B. Evans, *Fault mechanics and transport properties of rocks* (pp. 69-88). San Diego: Academic Press.

Morrow, C., Shi, L., & Byerlee, J. (1982). Strain hardening and strength of clay-rich fault gouges. *Journal of geophysical research*(87), 6771-6780.

Niemeijer, A., Spiers, C., & Peach, C. (2008). Frictional behaviour of simulated quartz fault gouges under hydrothermal conditions: Results from ultra-high strain rotary shear experiments. *Tectonophysics*(460), 288-303.

Ohtsubo, M., & Yoshimura, A. (1991). Particle interaction and rheology of illite-iron complexes. *Clay and Clay minerals*(39), 347-354.

Pillai, R. J., Robinson, R. G., & Boominathan, A. (2010). Shear Strength Behavior of Kaolinite with Different Microfabrics. *Indian Geotechnical Conference*.

Reinen, L., & Weeks, J. (1993). Determination of Rock Friction Consititutive Parameters using a Iterative Least Squares Inversion Method. *Journal of Geophysical Research*(98), 15937 - 15950.

Ruina, A. (1983, December). Slip Instability and State Variable Friction Laws. *Journal of Geophysical Research Vol 88*, 10359 - 10370.

Saffer, D., & Marone, C. (2003). Comparison of smectite- and illite rich gouge frictional properties: application to the updip limit of the seismogenic zone along subduction megathrusts. *Earth and Planetary Science Letters*(215), 219-235.

Salts Clay Minerals. (n.d.). Retrieved from http://www.saltsclaysminerals.com

Samuelson, J., & Niemeijer, A. R. (Unpublished results).

Samuelson, J., & Spiers, C. J. (2012). Fault friction and slip stability not affected by CO2 storage: Evidence from short-term laboratory experiments on North Sea reservoir sandstones anc caprocks. *International Journal of Greenhouse Gas Control*, S78-S90.

Scholz, C. (1998). Earthquakes and friction laws. *Nature*(391), 37-42.

Tembe, S., Lockner, D., & Wong, T.-F. (2010). Effect of clay content and mineralogy on frictional sliding behavior of simulated gouges: Binary and ternary mixtures of quartz, illite and montmorillonite. *Journal of Geophysical research*(115), B03416.

Warkentin, B. P., & Yong, R. (1960). Shear Strength of Montmorillonite and Kaolinite Related to Interparticle Forces. *Clays and Clay Minerals*(9), 210-218.

Zoback, M., & Gorelick, S. (2012). Earthquake triggering and large-scale geologic storage of carbon dioxide. *Proceedings of the National Academy of Science of the United States of America*, 10164–10168.

9. Appendix

Appendix 1: Constitutive parameters experiment u448 – Carmel

u448																					
Load (Mpa)	v0	v1	mu_o	stiffness	a	std a	b1	std b1	Dc1	std Dc1	b2	std b2	Dc2	std Dc2	a-b	btot	std btot	dctot	std dctot	lin_term	wc	law
20	0,001	0,01	0,50744	1,9	0,018359	0,000709	0,01074	0,000696	0,003825	0,000282	0	0	0	0	-0,00015	0,01074	0,000696	0,003825	0,000282	0	0,1	d
20	0,01	0,1	0,5053	0,5	0,009127	0,00008	0,001696	0,000441	0,042238	0,008119	0	0	0	0	-0,0008	0,001696	0,000441	0,042238	0,008119	0	0,1	d
25	0,001	0,01	0,49856	3	0,0129	0,000117	0,007476	0,000116	0,010379	0,00022	0,004513	3,40E-05	0,186186	0,00309	0,000911	0,011989	0,00015	0,196565	0,00331	0	0,1	d
25	0,01	0,1	0,50143	0,5	0,008341	0,000027	0,006558	0,000013	0,079443	0,000235	0,000753	1,34E-05	0,079891	0,002222	0,001029	0,007312	0,000027	0,159335	0,002458	0	0,1	d
30	0,001	0,01	0,51186	3	0,012294	0,00014	0,009146	0,000145	0,013332	0,000322	0,003992	7,69E-05	0,118391	0,002906	-0,00084	0,013138	0,000221	0,131723	0,003228	0,0263	0,1	d
30	0,01	0,1	0,53387	0,5	0,014169	0,00001	0,007538	0,00001	0,001067	0,000082	0,009178	2,02E-05	0,111102	0,000415	-0,00255	0,016716	0,000031	0,112169	0,000496	0,0314	0,1	d
35	0,001	0,01	0,54393	2,8	0,012231	0,000236	0,005063	0,001193	0,013683	0,002512	0,00457	0,001266	0,033667	0,004436	0,002598	0,009633	0,002459	0,04735	0,006949	0	0,1	d
35	0,01	0,1	0,55385	0,5	0,020772	0,000039	0,012557	0,000039	0,001095	0,000132	0,005935	7,67E-05	0,052778	0,000843	0,00228	0,018493	0,000116	0,053873	0,000975	0	0,1	d
40	0,001	0,01	0,55137	3	0,011817	0,000087	0,008338	0,000089	0,010678	0,000174	0,00404	5,12E-05	0,087091	0,001229	-0,00056	0,012378	0,000141	0,097769	0,001403	0,01	0,1	d
40	0,01	0,1	0,55926	0,5	0,018486	0,000011	0,010384	0,000011	0,001395	0,000046	0,005335	2,08E-05	0,062155	0,000308	0,002767	0,015719	0,000032	0,063549	0,000354	0,005	0,1	d
45	0,001	0,01	0,55958	3	0,009543	0,001227	-0,00067	0,001164	0,00302	0,039295	0	0	0	0	0,002329	-0,00067	0,001164	0,00302	0,039295	0,007	0,1	d
45	0,01	0,1	0,57116	0,5	0,008356	0,000055	0,004441	0,000054	0,054512	0,001063	0	0	0	0	0,003916	0,004441	0,000054	0,054512	0,001063	0	0,1	d
50	0,001	0,01	0,57258	3	0,012322	0,000178	0,009501	0,000177	0,013451	0,000321	0	0	0	0	0,002822	0,009501	0,000177	0,013451	0,000321	0	0,1	d
50	0,01	0,1	0,58381	0,5	0,010993	0,000011	0,003167	0,000011	0,002371	0,000181	0,006748	2,17E-05	0,073381	0,000307	0,001078	0,009915	0,000033	0,075752	0,000488	0	0,1	d
45	0,001	0,01	0,57711	3	0,014099	0,000248	0,010415	0,000248	0,011253	0,000391	0,002701	0,000104	0,126586	0,007904	0,000983	0,013116	0,000352	0,13784	0,008295	0	0,1	d
45	0,01	0,1	0,58116	0,5	0,008828	0,000035	0,005793	0,000077	0,054957	0,000839	0,005613	0,001087	0,517702	0,151402	-0,00258	0,011406	0,001164	0,572659	0,152241	0	0,1	d
40	0,001	0,01	0,55496	3	0,014948	0,000256	0,0128	0,000256	0,011648	0,000294	0	0	0	0	0,002148	0,0128	0,000256	0,011648	0,000294	-0,02	0,1	d
40	0,01	0,1	0,54312	0,5	0,00889	0,000049	0,00347	0,000084	0,033907	0,001075	0,004628	8,14E-05	0,132027	0,002376	0,000791	0,008098	0,000165	0,165934	0,003451	0	0,1	d
35	0,001	0,01	0,54049	3	0,019477	0,000474	0,011881	0,000418	0,003682	0,00021	0,007144	0,000216	0,024384	0,000664	0,000452	0,019025	0,000634	0,028066	0,000874	0	0,1	d
35	0,01	0,1	0,54347	0,5	0,00879	0,000041	0,003352	0,000059	0,0363	0,000915	0,008537	4,98E-05	0,167036	0,001432	-0,0031	0,01189	0,000109	0,203335	0,002348	0,0159	0,1	d
30	0,001	0,01	0,53309	3	0,016786	0,000218	0,012952	0,000213	0,007338	0,000183	0,004751	0,000116	0,061714	0,001718	-0,00092	0,017703	0,000329	0,069052	0,001901	0,0105	0,1	d
30	0,01	0,1	0,54416	0,5	0,022715	0,000018	0,014974	0,000018	0,001985	0,000062	0,007448	3,55E-05	0,092283	0,00066	0,000293	0,022422	0,000054	0,094268	0,000722	0	0,1	d
25	0,001	0,01	0,54108	3	0,019049	0,000457	0,013311	0,000449	0,005021	0,000205	0,006216	7,99E-05	0,198779	0,006151	-0,00048	0,019527	0,000529	0,203801	0,006356	0	0,1	d
25	0,01	0,1	0,54009	0,5	0,0183	0,000027	0,010466	0,000027	0,002744	0,000154	0,01039	5,03E-05	0,100141	0,000656	-0,00256	0,020857	0,000077	0,102885	0,00081	0,0136	0,1	d
20	0,001	0,01	0,58744	3	0,041955	0,000067	0,03148	0,000071	0,000853	0,000022	0,01008	0,000139	0,018109	0,000298	0,000399	0,041556	0,00021	0,018963	0,00032	0	0,1	d
20	0,01	0,1	0,59007	0,7	0,009817	0,000062	0,012616	0,000033	0,063451	0,001249	-0,00664	3,47E-05	0,081974	0,002669	0,003845	0,005972	0,000067	0,145425	0,003918	0	0,1	d

Appendix 2: Constitutive parameters experiment u450 – Carmel without hematite

u450																					
Load (Mpa)	v0	v1	mu_o	stiffness	a	std a	b1	std b1	Dc1	std Dc1	b2	std b2	Dc2	std Dc2	a-b	btot	std btot	dctot	std dctot	lin_term	wc	law
20	0,001	0,01	0,6475	3	0,014122	0,000165	0,009374	0,000169	0,020132	0,000555	0,005416	8,91E-05	0,235447	0,010639	-0,00067	0,01479	0,000259	0,255579	0,011193	0	0,1	d
20	0,01	0,1	0,64753	0,5	0,009379	0,000066	0,006885	0,000344	0,076239	0,002593	0	0	0	0	-0,00393	0,006885	0,000344	0,076239	0,002593	0	0,1	d
25	0,001	0,01	0,6317	3	0,029671	0,000074	0,01822	0,000077	0,00073	0,000043	0,007791	0,00015	0,015595	0,000338	0,00366	0,026012	0,000227	0,016325	0,000381	-0,01	0,1	d
25	0,01	0,1	0,63356	0,5	0,019859	0,000013	0,012003	0,000013	0,001343	0,000067	0,009188	2,46E-05	0,123785	0,000596	-0,00133	0,021191	0,000037	0,125129	0,000664	0	0,1	d
30	0,001	0,01	0,6118	3	0,013347	0,000105	0,009276	0,000109	0,012878	0,000229	0,002584	5,82E-05	0,112459	0,003238	0,001488	0,01186	0,000167	0,125337	0,003467	0	0,1	d
30	0,01	0,1	0,61572	0,5	0,015419	0,000009	0,008965	0,000009	0,001738	0,000054	0,007394	1,79E-05	0,119947	0,000624	-0,00094	0,016359	0,000027	0,121685	0,000678	0	0,1	d
35	0,001	0,01	0,60177	3	0,014066	0,000101	0,009261	0,000108	0,017724	0,000319	0,002807	0,000119	0,194634	0,020482	0,001998	0,012068	0,000227	0,212358	0,020801	0	0,1	d
35	0,01	0,1	0,60614	0,5	0,013806	0,000016	0,005823	0,000016	0,000742	0,000184	0,00985	3,06E-05	0,088145	0,000433	-0,00187	0,015673	0,000046	0,088888	0,000617	0	0,1	d
40	0,001	0,01	0,59418	3	0,01409	0,000126	0,008519	0,000125	0,006235	0,000141	0,004145	7,67E-05	0,043217	0,000796	0,001426	0,012664	0,000201	0,049453	0,000937	0	0,1	d
40	0,01	0,1	0,59312	0,5	0,007615	0,000051	0,004621	0,000981	0,054055	0,004639	0,003991	0,000972	0,106082	0,011517	-0,001	0,008612	0,001953	0,160138	0,016156	0	0,1	d
45	0,001	0,01	0,59088	3	0,01265	0,000191	0,009022	0,000205	0,011377	0,000402	0,002749	0,000139	0,077446	0,004055	0,000879	0,011771	0,000344	0,088823	0,004457	0	0,1	d
45	0,01	0,1	0,59272	0,5	0,012165	0,000024	0,006336	0,000025	0,003373	0,000244	0,006389	4,72E-05	0,081163	0,000855	-0,00056	0,012724	0,000072	0,084535	0,001099	0	0,1	d
50	0,001	0,01	0,59671	3	0,013604	0,000155	0,009678	0,000159	0,008344	0,000213	0,003274	9,96E-05	0,062204	0,001953	0,000653	0,012952	0,000259	0,070548	0,002166	0	0,1	d
50	0,01	0,1	0,59559	0,5	0,006994	0,000026	0,005206	0,000029	0,051548	0,000461	0,009393	4,43E-02	0,740561	0,003041	-0,00761	0,014599	0,000074	0,792109	0,003501	0	0,1	d
45	0,001	0,01	0,60106	3	0,013313	0,000225	0,011293	0,000225	0,01256	0,000351	0,004894	0,000125	0,266497	0,016257	-0,00287	0,016187	0,000349	0,279057	0,016608	0	0,1	d
45	0,01	0,1	0,59569	0,5	0,006533	0,000028	0,006302	0,000094	0,060616	0,00084	0,003315	0,000125	0,304316	0,034698	-0,00308	0,009618	0,000219	0,364932	0,035537	0	0,1	d
40	0,001	0,01	0,58957	3	0,015632	0,000177	0,012806	0,000175	0,007969	0,000145	0,006881	4,77E-05	0,179865	0,002717	-0,00406	0,019687	0,000223	0,187834	0,002862	0	0,1	d
40	0,01	0,1	0,5801	0,5	0,006578	0,000026	0,006029	0,00005	0,053887	0,000542	0	0	0	0	-0,01189	0,006029	0,00005	0,053887	0,000542	0	0,1	d
35	0,001	0,01	0,57313	3	0,015935	0,000273	0,013063	0,000271	0,010633	0,000308	0	0	0	0	-0,00427	0,013063	0,000271	0,010633	0,000308	0	0,1	d
35	0,01	0,1	0,56399	0,5	0,007303	0,000034	0,005497	0,000044	0,039534	0,000467	0	0	0	0	-0,00894	0,005497	0,000044	0,039534	0,000467	0	0,1	d
30	0,001	0,01	0,56135	3,5	0,015875	0,000185	0,014127	0,000184	0,010115	0,000176	0	0	0	0	-0,00943	0,014127	0,000184	0,010115	0,000176	0	0,1	d
30	0,01	0,1	0,54801	0,5	0,007634	0,000066	0,005078	0,000079	0,02904	0,000693	0	0	0	0	-0,00662	0,005078	0,000079	0,02904	0,000693	0	0,1	d
25	0,001	0,01	0,56696	3	0,01526	0,000251	0,014167	0,000252	0,01242	0,000315	0	0	0	0	-0,00619	0,014167	0,000252	0,01242	0,000315	0	0,1	d
25	0,01	0,1	0,55121	0,5	0,00703	0,000047	0,006859	0,00009	0,045843	0,000742	0	0	0	0	-0,00689	0,006859	0,00009	0,045843	0,000742	0	0,1	d
20	0,001	0,01	0,57886	3	0,015222	0,000308	0,013573	0,000307	0,010565	0,000342	0,006096	0,000111	0,159633	0,005471	-0,00445	0,019669	0,000419	0,170198	0,005813	0	0,1	d
20	0,01	0,1	0,56712	0,7	0,008444	0,000031	0,008915	0,000046	0,043107	0,00031	0	0	0	0	-0,01034	0,008915	0,000046	0,043107	0,00031	0	0,1	d